

Inducing exceptional points, enhancing plasmon quality and creating correlated plasmon states with modulated Floquet parametric driving

Egor I. Kiselev,^{1,2} Mark S. Rudner,³ and Netanel H. Lindner¹

¹*Physics Department, Technion, 320003 Haifa, Israel*

²*The Helen Diller Quantum Center, Technion, Haifa 3200003, Israel*

³*Department of Physics, University of Washington, Seattle, Washington 98195-1560, USA*

We propose a method to parametrically excite low frequency collective modes in an interacting many body system using a Floquet driving at optical frequencies with a modulated amplitude. We demonstrate that it can be used to design plasmonic time-varying media with singular dispersions. Plasmons near resonance with half the modulation frequency exhibit two lines of exceptional points connected by dispersionless states. Above a critical driving strength, resonant plasmon modes become unstable and undergo a continuous transition towards a crystal-like structure stabilized by interactions and nonlinearities. This new state breaks the discrete time translational symmetry of the drive as well as the translational and rotational spatial symmetries of the system and exhibits soft, Goldstone-like phononic excitations. Below the instability threshold, our method can be used to enhance the quality of plasmon resonances.

I. INTRODUCTION

The collective modes of a many-body system fingerprint the symmetries underlying a phase of matter. They also play an important role in transitions to non-equilibrium states when the system is subjected to an external drive. Resonantly driving collective modes can lead to exotic wave propagation effects and, at strong driving, to instabilities leading to new symmetry breaking non-equilibrium states [1–5]. An example for such an instability in classical physics is Faraday waves formed by parametrically driven surface waves [6–8].

Accessing such phenomena in electronic systems is challenging due to a lack of methods for the control and manipulation of collective modes in solids. At the same time, realizing such control holds a lot of promise for applications in fields like plasmonics or spintronics. Here, we show that Floquet engineering, which employs driving at optical frequencies to manipulate electronic bandstructures [9–38], can be an effective tool to control collective modes. We focus on plasmons in clean, two dimensional materials which exhibit large quality factors due to the absence of impurity scattering and the suppression of Landau damping by the \sqrt{q} shape of their dispersion. We demonstrate that optical driving fields, far off-resonant relative to the plasmon frequencies, can lead to the formation of exceptional points and non-dispersive plasmonic states through a parametric coupling mechanism which we call “modulated Floquet parametric driving” (MFPD). For strong driving, we predict the existence of an emergent non-equilibrium state with spatio-temporal correlations that break time and space translation symmetry. This connects to the ongoing interest in using complex multi-component driving signals to control solid-state electrons [38–41] and to induce non-equilibrium correlated states [5, 23, 42–48]. Furthermore we show that MFPD can be used to increase plasmon quality factors.

MFPD takes advantage of the fact that the electronic

properties of two dimensional materials are modified in the presence of a high frequency time-periodic driving fields [49]. Slowly modulating the parameters of these fields, an electronic system can be controlled dynamically. As illustrated in Fig.1a), a high-frequency Floquet driving alters the shape of the quasi-energy bands (red curves). In particular, the effective mass m^* of electrons at the Fermi surface changes. This change results in an altered plasmon dispersion. A periodic modulation of the Floquet drive’s amplitude results in a periodically changing mass that parametrically excites plasmon modes. This effect induces two lines of exceptional points in the plasmon dispersion [Fig.1b)]. These exceptional lines are separated by a non-dispersive gap where the real part of the plasmon dispersion is flat. Inside the gap, damping, which is reflected in the negative imaginary part of the plasmon dispersion, is reduced by MFPD. This effect can be used to enhance the quality of the plasmon resonance and increase plasmonic propagation lengths.

For sufficiently strong driving, for plasmons with wavenumbers q^* meeting the condition $\text{Re}[\omega_{\text{pl}}(q^*)] = \omega_1$, where $\omega_{\text{pl}}(q)$ is the plasmon dispersion and $2\omega_1$ is the amplitude modulation frequency, the imaginary part of the dispersion changes sign. These plasmons become unstable and, after a short period of exponential growth, form a crystal-like lattice with a periodically modulated electron density [Fig.1 c)]. The structure of this crystal is determined by the nonlinearities of the system. The density oscillates at half the modulation frequency, thus breaking the π/ω_1 discrete time translation symmetry of the drive – a behavior known in discrete time crystals [45–48, 50–54].

An important challenge in Floquet engineered systems is heating [55–69]. Here, we show that the parametric excitation of plasmons by MFPD can be achieved in an off-resonant regime where (momentum conserving) single-photon excitation of electrons is blocked. To achieve this, the base-tone drive frequency Ω_F and the Fermi energy

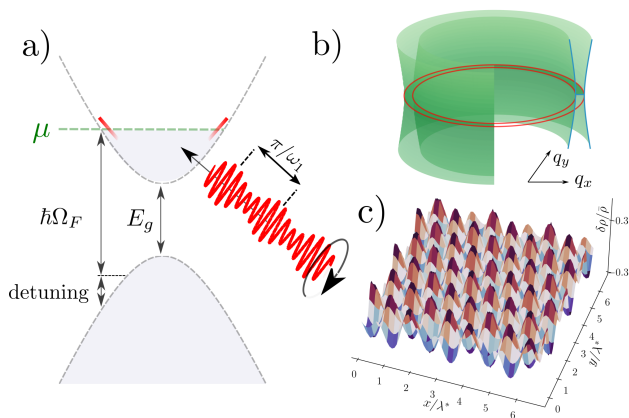


Figure 1. Modulated Floquet parametric driving, exceptional lines and non-equilibrium steady states: a) Illustration of the quasi-energy bands of electrons in a gapped system under MFPD. The dashed gray lines represent the undriven band structure. A Floquet signal with the frequency Ω_F , where $\hbar\Omega_F > E_g$, is applied. The quasi-energy bands in the vicinity of the Fermi surface for a non-zero driving amplitude are shown in red. By modulating the amplitude of the fast Floquet drive with a frequency $2\omega_1$, an oscillation of the dispersion and the effective mass of the electrons at the Fermi level is induced (see Eq. (6)). b) The periodic modulation of the Fermi velocity induces two lines of exceptional points (shown as red circles) in the rotationally symmetric dispersion of the soft THz plasmon mode (green surfaces) – see Fig. 2 for an in-detail cross-sectional view. c) Above a critical value, the mass oscillation parametrically excites THz plasmons. Due to nonlinear and interaction effects, the plasmons arrange themselves in a crystal-like structure whose periodicity is determined by the condition $\omega_1 = \omega_{\text{pl}}(q^*)$, where $\omega_{\text{pl}}(q)$ is the plasmon dispersion. The crystalline state breaks the rotational and translational symmetries of the undriven system and supports soft phonon-like Goldstone modes.

μ must be chosen such that all electronic states supporting a resonant interband single photon excitation with an energy transfer of $\hbar\Omega_F$ and near-zero momentum transfer lie below the Fermi surface (see shaded regions Fig. 1). Processes involving multiple photons are suppressed in the small ratio of drive amplitude and drive frequency, leading to strongly reduced heating rates due to photoexcited electrons. We estimate the heating due to momentum non-conserving absorption mediated by phonons or impurity-scattering, as well as interaction assisted processes, and find that the heating rates are small, such that they can be balanced by the cooling power of the crystal lattice.

Below, we describe in more detail the creation of singular plasmon dispersions and the excitation of plasmonic instabilities by MFPD, the transition into the crystalline state and the propagation of Goldstone-like, phononic collective modes in the symmetry broken state.

II. RESULTS

A. Modulated Floquet parametric driving

The idea of MFPD is to use the dependence of the quasi-energy band structure on the parameters of the drive to couple to the soft collective modes of the system. We show how the slow modulation of the driving amplitude leads to a time-varying effective electron mass. For concreteness, let us consider a coherently driven, gapped 2D Dirac system described by the Hamiltonian

$$H = \sum_{\mathbf{k}} \mathbf{c}_{\mathbf{k}}^\dagger [H_0(\mathbf{k}) + H_d(t)] \mathbf{c}_{\mathbf{k}} + \sum_{\mathbf{q}} V(\mathbf{q}) \hat{\rho}_{\mathbf{q}} \hat{\rho}_{-\mathbf{q}}. \quad (1)$$

We will first illustrate how the external drive modifies the dispersion in a single valley. The dispersion in the opposite valley is modified similarly. Both valleys will be taken into account when considering the collective modes. For small values of \mathbf{k} around the center of the valley, we have $H_0 = \mathbf{d} \cdot \boldsymbol{\sigma}$, where $\mathbf{d} = [\lambda k_x, \lambda k_y, E_g/2]$, $\boldsymbol{\sigma}$ is a Pauli matrix vector describing the orbital pseudospin degree of freedom and E_g is the energy gap between the two bands. $\mathbf{c}_{\mathbf{k}}^\dagger$ ($\mathbf{c}_{\mathbf{k}}$) are two-component electron creation (annihilation) operators, where individual components describe electrons with different pseudospin orientations, and $H_d(t) = e\mathbf{A}(t) \cdot \nabla_{\mathbf{k}} H_0$ is the driving Hamiltonian derived from minimal coupling.

We assume circularly polarized light with an amplitude \mathcal{E} described by $\mathbf{A}(t) = (\mathcal{E}/\Omega_F) [-\sin \Omega_F t, \cos \Omega_F t, 0]$. The 2D Fourier transform of the Coulomb potential is given by $V(\mathbf{q}) = 2\pi/q$ and $\hat{\rho}_{\mathbf{q}} = \sum_{\mathbf{k}} \mathbf{c}_{\mathbf{k}}^\dagger \mathbf{c}_{\mathbf{k}+\mathbf{q}}$ is the density operator. We emphasize that we use the gapped Dirac Hamiltonian of Eq. (1) as an example. The physics presented here does not depend on the precise band structure of the system.

It is convenient to work in a rotating frame defined by the unitary transformation $U(t) = e^{i\mathbf{d} \cdot \boldsymbol{\sigma} \Omega_F t/2}$, where the spectrum of the transformed single-particle part of Eq. (1) is given by

$$\varepsilon_{\mathbf{k}} \approx \sqrt{\left(|\mathbf{d}| - \frac{\hbar\Omega_F}{2}\right)^2 + \frac{e^2 \mathcal{E}^2 \lambda^2}{4\Omega_F^2 \hbar^2} \left(2 - \frac{E_g}{|\mathbf{d}|}\right)} \quad (2)$$

for $\lambda k/|\mathbf{d}| \ll 1$. In writing Eq. (2) we neglected time dependent terms in the rotating frame [11]. In this frame and with the approximations made, the time dependence caused by the fast Ω_F oscillation of the Floquet drive does not explicitly appear in the equations.

We consider the metallic regime with the Fermi surface lying in the upper band (see Fig. 1) and expand the spectrum around k_F – the Fermi momentum of the undriven system. We write:

$$\varepsilon_{\mathbf{k}} \approx \hbar v_F(\mathcal{E}, \Omega_F)(k - k_F) + \varepsilon_{k_F}(\mathcal{E}, \Omega_F) \quad (3)$$

The Fermi velocity $v_F(\mathcal{E}, \Omega_F)$ depends on the amplitude and frequency of the Floquet drive.

A variation of the drive amplitude \mathcal{E} results in a small change of the dispersion $\varepsilon_k \rightarrow \bar{\varepsilon}_k + \delta\varepsilon_k$ near the Fermi surface. To clearly distinguish between constant quantities and quantities oscillating with the slow modulation frequency ω_1 , here and in the following, we write the constant part with a bar. The total charge of the system is conserved and therefore k_F is fixed. However, the slope of ε_k at k_F and therefore the effective mass of the electrons $m^* = \hbar k_F / v_F(\mathcal{E}, \Omega_F)$ are altered. For a small $\delta\varepsilon_k$, we find

$$\bar{\varepsilon}_k + \delta\varepsilon_k \approx \left(1 - \frac{\delta m^*}{\bar{m}^*}\right) \frac{\hbar^2 k_F}{\bar{m}^*} (k - k_F). \quad (4)$$

We consider a slow, adiabatic oscillation of the electric field amplitude \mathcal{E} ,

$$\mathcal{E}(t) = \bar{\mathcal{E}} + \delta\mathcal{E} \cos(2\omega_1 t), \quad (5)$$

such that $\omega_1 \ll \Omega_F$. This slow oscillation does not couple to any single-electron degrees of freedom. However, as demonstrated below, it does couple to the soft plasmon mode through a parametric resonance induced by the periodic change of the effective mass

$$m^*(t) = \bar{m}^* \left(1 + \frac{\delta m^*(t)}{\bar{m}^*}\right). \quad (6)$$

B. Equations of motion for collective dynamics

To describe the electron dynamics of MFPD driven plasmons, we use a hydrodynamic description of Coulomb interacting electrons (see, e.g., Refs. [70–72]). The equations of motion follow from the conservation of charge and momentum [73–75]. The continuity equation for the electron density ρ is

$$\partial_t \rho(t, \mathbf{x}) = -\partial_i [\rho(t, \mathbf{x}) u_i(t, \mathbf{x})], \quad (7)$$

where $\mathbf{u}(t, \mathbf{x})$ is the electron flow velocity. The continuity equation for the momentum density is given by the Euler equation

$$\partial_t (m^* \rho u_i) + \partial_j \Pi_{ij} = -\gamma m^* \rho u_i - e \rho \partial_i \phi, \quad (8)$$

where $m^* = \hbar k_F / v_F$ is the effective mass of electrons at the Fermi surface, given by the ratio of Fermi momentum $\hbar k_F$ and Fermi velocity v_F , u_i is the electron flow velocity, and γ is the rate of momentum relaxation, e.g., due to impurity or phonon scattering. The stress tensor Π_{ij} is given by

$$\Pi_{ij} = m^* \rho u_i u_j + \delta_{ij} p, \quad (9)$$

where p is the pressure. The electrostatic potential is given by

$$\phi(t, \mathbf{x}) = \int d^2 x' \frac{e \rho(t, \mathbf{x}')}{4\pi \varepsilon |\mathbf{x} - \mathbf{x}'|}. \quad (10)$$

Here e is the electron charge and ε the effective dielectric constant. Solutions of equations (7) and (8) describe the collective oscillations of the electron fluid.

C. Oscillating mass

The oscillating mass increment $\delta m^*(t)$ in Eq. (8) acts as a parametric drive, which is known to lead to instabilities [76]. In the following we identify the parametric instability of the charge density ρ . It is convenient to take the divergence of Eq. (8) and to combine the result with the continuity equation (7), including the drive-induced temporal modulation of $m^*(t)$. Doing so, we find

$$\partial_t m^*(t) \partial_t \rho + \gamma m^*(t) \partial_t \rho - m^*(t) \partial_i \partial_j \rho u_i u_j = \partial_i \rho \partial_i \phi, \quad (11)$$

where we neglected the pressure term p since its contribution is subleading to the long-range Coulomb potential [77, 78][79]. Unless otherwise indicated, throughout the paper, derivatives act on all functions to the right. In our derivations, we also neglect the time dependent contribution to the damping term, which is negligible in comparison to the static one.

D. Instabilities and exceptional points

In this section, we present how the oscillating mass under MFPD in Eq.(6) influences the plasmon dynamics under Eq. (11). Consider the electron density $\rho = \bar{\rho} + \delta\rho$, where $\bar{\rho}$ is the equilibrium electron density and $\delta\rho$ is a perturbation of $\bar{\rho}$. To linear order in $\delta\rho$, and performing a Fourier transform $\mathbf{x} \rightarrow \mathbf{q}$, for a modulation $\delta m^*(t) / \bar{m}^* = h \cos(2\omega_1 t)$, we obtain from Eq. (11)

$$\partial_t (1 + h \cos(2\omega_1 t)) \partial_t \delta\rho_q + \gamma \partial_t \delta\rho_q + \omega_{\text{pl}}^2(q) \delta\rho_q = 0. \quad (12)$$

The plasmon dispersion is given by

$$\omega_{\text{pl}}(q) = \sqrt{\frac{e \bar{\rho}}{4\pi \bar{m}^* \varepsilon} q^2 V(q)}. \quad (13)$$

The parameter γ captures scattering on impurities and lattice excitations, which lead to damping of the plasmon modes. Intrinsic Landau damping is strongly suppressed for the wavenumbers and frequencies under consideration, since they lie outside of the particle-hole continuum. Indeed, recent experiments on high quality graphene showed that damping mainly arises due to scattering with phonons [80]. It is important to note that this scattering mechanism is strongly suppressed at low temperatures, where dissipation is dominated by losses caused by electric fields penetrating into the substrate [80]. In general, it is believed that substrate engineering and strong cooling could strongly increase the plasmon quality [81]. Notice that Eq. (12) is equivalent to the equation describing the propagation of the magnetic field in photonic time crystals [82].

In Sec. IV A, we derive a solution for $\delta\rho_q$ using the slowly varying envelope approximation, which is valid near the parametric resonance where $\omega_{\text{pl}}^2(q) \approx \omega_1$:

$$\delta\rho_q(t) = a_q(t) \cos(\omega_1 t) + b_q(t) \sin(\omega_1 t). \quad (14)$$

Here the amplitudes are given by $a_q(t) = a_q(0)e^{s_{\pm}(q)t}$ and $b_q(t) = b_q(0)e^{s_{\pm}(q)t}$, where

$$s_{\pm}(q) = -\frac{\gamma}{2} \mp i\frac{\omega_1}{2} \sqrt{\frac{[\omega_{\text{pl}}^2(q) - \omega_1^2]^2}{\omega_1^4} - \left(\frac{h}{2}\right)^2}. \quad (15)$$

We now examine the plasmon dispersion in the presence of parametric driving. To this end, it is convenient to rewrite Eq. (14): according to Floquet's theorem, any solution to Eq. (12) can be written in the form $\delta\rho_q = e^{-i\Lambda(q)t}u_{\Lambda}(t)$, where $u_{\Lambda}(t + \pi/\omega_1) = u_{\Lambda}(t)$. Choosing $u_{\Lambda}(t) = [a_{\Lambda_{\pm}(q)}(e^{2i\omega_1 t} + 1) - ib_{\Lambda_{\pm}(q)}(e^{2i\omega_1 t} - 1)]/2$, and comparing to Eq. (14), we obtain a correspondence between $\Lambda(q)$ and $s(q)$ giving the plasmon dispersion close to the resonance:

$$\Lambda_{\pm}(q) = is_{\pm}(q) + \omega_1. \quad (16)$$

Note that the Floquet exponent $\Lambda(q)$ is defined modulo $2\omega_1$ (because a change by $2\omega_1$ can always be absorbed into $u_{\Lambda}(t)$). In analogy to the Bloch theory of electronic band structure, $2\omega_1$ plays the role of a reciprocal lattice vector.

While Eqs. (15) and (16) are valid near $\omega_{\text{pl}}(q) = \omega_1$, for small q , keeping higher order derivatives neglected above in the slowly varying envelope approximation, and ignoring damping, we find that the two branches of the plasmon dispersion are given by $\Lambda_+(q) \approx 2\omega_1 - \omega_{\text{pl}}(q)/\sqrt{1+h^2/4}$ and $\Lambda_-(q) \approx \omega_{\text{pl}}(q)/\sqrt{1+h^2/4}$. For the Λ_- branch, we find $b_{\Lambda_-(q=0)} = ia_{\Lambda_-(q=0)}$, giving $\delta\rho_q \approx a_{\Lambda_-(q=0)}e^{i\omega_{\text{pl}}(q)t/\sqrt{1+h^2/4}}$. Therefore, the Λ_- branch describes a counter-propagating mode with the frequency $-i\omega_{\text{pl}}(q)/\sqrt{1+h^2/4}$, lifted by one reciprocal lattice vector $2\omega_1$. We conclude that, away from the resonance, the parametric driving influences the plasmons only weakly. The plasmon dispersion in the presence of parametric driving $\Lambda(q)$ is shown in Fig. 2.

Exceptional points appear at wavenumbers q_{exc} , where the \pm -branches of $s_{\pm}(q)$ merge, i.e., when the condition $\omega_{\text{pl}}^2(q_{\text{exc}}) = \omega_1^2(1 \pm h/2)$ is met. This results in a diverging group velocity $\partial s_{\pm}(q)/\partial q \sim |q - q_{\text{exc}}|^{-1/2}$ for $q \rightarrow q_{\text{exc}}$. In the interval between the two exceptional points q_{exc} , $s_{\pm}(q)$ is purely real. This corresponds to non-dispersive plasmons, oscillating at frequency ω_1 (see Fig. 2).

Let us now consider the stability of plasmon modes under MFPD. The instability condition $\text{Re}(s) > 0$ is realized for $h > 2\gamma/\omega_1$ in a narrow frequency range around $\omega_{\text{pl}}(q) = \omega_1$ given by

$$[\omega_{\text{pl}}^2(q) - \omega_1^2]^2 < \omega_1^4 h^2/4 - \omega_1^2 \gamma^2. \quad (17)$$

The fastest growing modes have wavenumbers q^* determined by the condition

$$\pm\omega_{\text{pl}}(q^*) = \omega_1. \quad (18)$$

Thus, the parametric driving will excite plasmons with the frequency ω_1 , whose amplitude will grow according

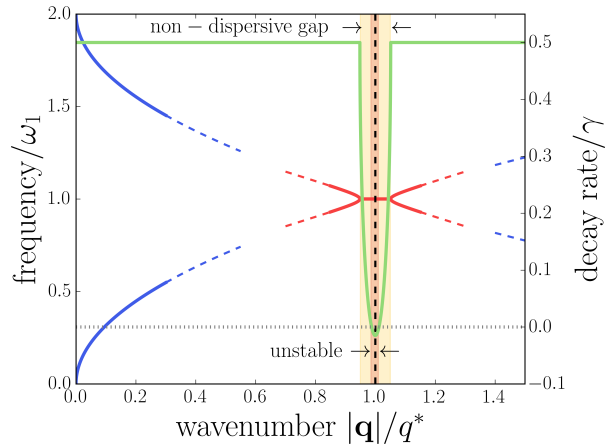


Figure 2. Onset of the plasmon instability induced by modulated Floquet parametric driving with the modulation frequency $2\omega_1$. Red and blue lines show the the quasi-energy dispersion $\text{Re}[\Lambda(q)]$ of parametrically driven plasmons (see Eq. (16) and discussion below). Far away from the critical q^* , 2D plasmons retain the characteristic square-root shape of their dispersion relation (blue lines). The quasi-energy dispersion is invariant with respect to shifts by $2\omega_1$ – the reciprocal lattice constant in frequency space. Near q^* , where $\omega_{\text{pl}}(q^*) \approx \omega_1$ holds, the dispersion is strongly altered by the driving (red lines). A gap which hosts non-dispersive modes opens around q^* (yellow shading). Merging branches of the dispersion at the edges of the non-dispersive gap indicate exceptional points with diverging group velocities. We chose the modulation amplitude h to lie slightly above the instability threshold: damping is negative in a small interval around q^* , leading to an exponential growth of unstable modes (red shading). However, exceptional points and non-dispersive states appear even for subcritical driving strengths.

to $\delta\rho_{q^*} \sim e^{(h\omega_1/4 - \gamma/2)t}$. Notice that the system's response breaks the discrete time translation symmetry of the drive with respect to translations by $T = \pi/\omega_1$.

The periodic driving opens a vertical non-dispersive gap around q^* , where the two branches of the plasmon dispersion meet. Inside the gap, the real part of $\Lambda_{\pm}(q)$ is flat. This phenomenon is known from photonic time varying media and photonic time crystals, where it is often referred to as momentum-gap or k-gap [82, 83]. In fact, Eq. (12) maps onto the equation describing the propagation of light through a photonic time crystal [82]. The full plasmon dispersion near the onset of the instability ($h\omega_1/4 \gtrsim \gamma/2$) is illustrated in Fig. 2.

E. Enhancing plasmonic quality factors

In this section, we show how MFPD below the instability threshold can be used to enhance plasmonic quality factors. As an example we consider a plasmon source that is located at $x = 0$ and is, for simplicity, uniform along the y -axis, which is a reasonable approximation for

a strip whose width is shorter than the plasmon wavelength [84]. This source is placed into an MFPD driven plasmonic medium. We use Eq. (12) with a pointlike source term oscillating at frequency ω_1 added to the left hand side to analyze plasmon propagation in this setting. In the Supplementary Information, we show that for any fixed $t \rightarrow \infty$, the plasmon amplitude away from the source behaves as

$$\delta\rho(x) \sim \delta\rho(0) e^{-\frac{q^*}{\mathcal{Q}(h)}|x|}, \quad (19)$$

where

$$\mathcal{Q}(h) = \frac{1}{\sqrt{\gamma^2/\omega_1^2 - h^2/4}} \quad (20)$$

is the plasmon quality factor. In the absence of MFPD, $\mathcal{Q}(h)$ reduces to the well known expression $\mathcal{Q}(h=0) = \omega_1/\gamma$. Eq. (20), shows that for driving strengths h close to, but below the instability threshold $h_c = 2\gamma/\omega_1$, the quality of the plasmon resonance can be strongly enhanced. To demonstrate the enhancement, we perform a numerical simulation of Eq. (12). For all simulations in this paper we use the Dedalus spectral solver [85]. The results (see Fig. 3) show a good agreement with Eq. (19), and demonstrate that a significant enhancement of \mathcal{Q} can be achieved at driving strengths below the instability threshold. This opens the possibility of enhancing the quality of plasmon resonances with high frequency optical drives.

Finally, we note that the quality factor \mathcal{Q} depends on temperature. In experiments with graphene plasmons, \mathcal{Q} roughly decreases by a factor of two when the temperature is raised from 100 K to 200 K [80]. Below, we estimate that the temperature raise induced by MFPD is on the order of a few tens of Kelvin for $h = h_c$. Thus MFPD can compensate for the heating induced lowering of \mathcal{Q} , if h is chosen close to h_c .

F. Crystallization

We now turn to describing pattern formation that occurs for MFPD above the critical driving threshold, $h > h_c$. Having identified the wavenumber q^* of the unstable modes in Eqs. (13) and (18), we now study the steady state spatial structure of the plasmon charge density once the initial exponential growth has been saturated by the nonlinearities. We use the nonlinear equation of motion for plasmons with an oscillating mass term, Eq. (11), derived in Sec. II C. For simplicity, we focus on a quasi 1D strip whose width along the y -direction is smaller than the plasmon wavelength $\lambda^* = 2\pi/q^*$. These boundary conditions are implemented by setting $\rho = 0$ outside the strip.

Parametrically driven nonlinear waves were thoroughly studied in nonlinear spin and optical systems in the context of wave turbulence [86]. In general, the saturation of unstable modes can be described within the subspace of

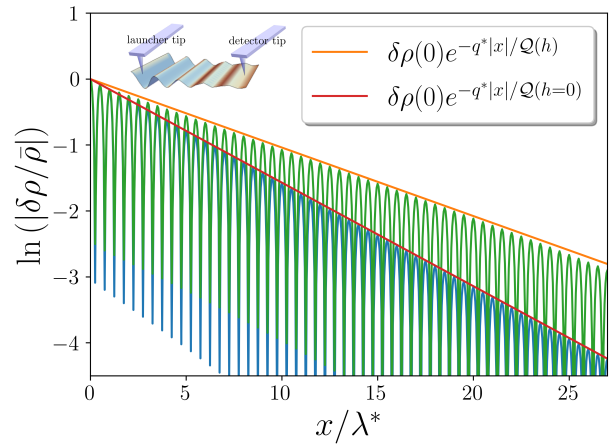


Figure 3. Enhancement of the plasmon quality factor by MFPD (logarithmic plot). A source at $x = 0$ induces plasmons propagating along the x -axis. The plasmon amplitude is exponentially damped according to Eq. (19). Blue and green curves show the plasmon wave with MFPD switched on and off, respectively. The enhancement of the plasmon quality factor shows in a larger propagation length and agrees well with the prediction of Eq. (20). A driving strength of $h = 0.75h_c$ was used in the simulation.

modes that satisfy the condition $2\omega_1 = \omega_{\text{pl}}(q) + \omega_{\text{pl}}(-q)$ [86]. For the strip geometry, where q_y is fixed to zero, these are precisely the linearly unstable modes of Eqs. (14) and (34). Physically, the above condition reflects that the uniform parametric driving cannot supply momentum to the system, and plasmons can only be created in pairs with wavenumbers $q_x = \pm q^*$. Thus, the saturation to the final steady state will be captured by the ansatz

$$\delta\rho_s(t, y) = a(t) \cos(\omega_1 t) \cos(q^* \cdot x) + b(t) \sin(\omega_1 t) \cos(q^* \cdot x). \quad (21)$$

A similar instability appears in parametrically driven shallow water waves, so called Faraday waves [6–8, 87–90]. The Faraday instability has also been reported for cold atom systems [91, 92] and Luttinger liquids [93].

As shown in Sec. IV B inserting the ansatz of Eq. (21) into the plasmon equation of motion (11) leads to the set of amplitude equations

$$\begin{aligned} \dot{a} &= -\alpha b - \frac{1}{2}\gamma a + \beta b(a^2 + b^2) \\ \dot{b} &= -\alpha a - \frac{1}{2}\gamma b - \beta a(a^2 + b^2), \end{aligned} \quad (22)$$

with $\alpha = \omega_1 h/4$ and $\beta = \omega_1/32(\bar{\rho})^2$. To gain an intuition for the steady state, it is useful to consider the fixed point, where $\dot{a}(a_{\text{fp}}, b_{\text{fp}}) = \dot{b}(a_{\text{fp}}, b_{\text{fp}}) = 0$ and solve for the amplitude $r_{\text{fp}}^2 = a_{\text{fp}}^2 + b_{\text{fp}}^2$. Here, the subscript “fp” stands for values at the fixed point. One finds

$$r_{\text{fp}}^2 = a_{\text{fp}}^2 + b_{\text{fp}}^2 = \frac{\alpha}{\beta} \sqrt{\left[1 - \left(\frac{\gamma}{2\alpha}\right)^2\right]}. \quad (23)$$

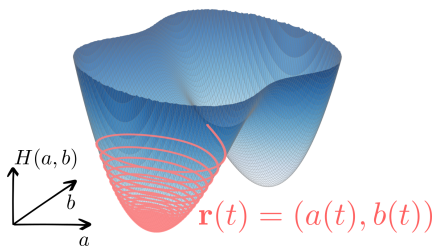


Figure 4. The effective Hamiltonian of Eq. (24) in amplitude space, with the two minima corresponding to symmetry breaking states. The red trajectory is a solution to Eqs. (22) and shows the transition to the crystalline state in the presence of damping.

This expression indicates a critical point at $h_c = 2\gamma/\omega_1$, beyond which, for $h > h_c$, physically meaningful fixed points with a real, finite amplitude r_{fp} exist. Equation (23), also shows that the amplitude r_{fp} has two distinct scaling regimes connected by a crossover. For large h , the damping γ is negligible and $r_{\text{fp}} \approx \sqrt{\alpha/\beta}$. On the other hand, close to the critical point h_c , we find $r_{\text{fp}} \approx \sqrt{\alpha_c/\beta} (2\epsilon)^{1/4}$, where $\epsilon = (\alpha - \alpha_c)/\alpha_c$ with $\alpha = \omega_1 h_c/4$. We will refer to these two cases as the weakly damped and the strongly damped, respectively. In what follows, we use Eqs. (22) to study the transition to the crystalline non-equilibrium steady state in both cases.

1. Transition in the weakly damped case

For $\gamma = 0$, the Eqs. (22) correspond to the equations of motion arising from the Hamiltonian

$$H(a, b) = \frac{1}{2}\alpha(a^2 - b^2) + \frac{1}{4}\beta(a^4 + b^4) + \frac{1}{2}\beta a^2 b^2. \quad (24)$$

Similar Hamiltonians are obtained for nonlinear parametric oscillators in both quantum and classical limits [94, 95]. The stable minima of the Hamiltonian (24) are located at:

$$a_* = 0, \quad b_* = \pm \sqrt{\frac{\alpha}{\beta}}, \quad (25)$$

In the presence of weak damping, Eqs. (22) predict that, for any initial condition, the trajectory $r(t) = (a(t), b(t))$ will descend to one of the minima predicted by Eq. (25) (see Fig. 4). The steady state will be a standing wave of the form of Eq. (21) with the amplitude given by Eq. (25).

We note that noise can significantly alter the dynamics of the plasmon modes. It can, e.g., lead to transitions between the two minima of the Hamiltonian (24) [94]. In the case of multiple non-degenerate minima noise can determine the ultimate stable configuration [94].

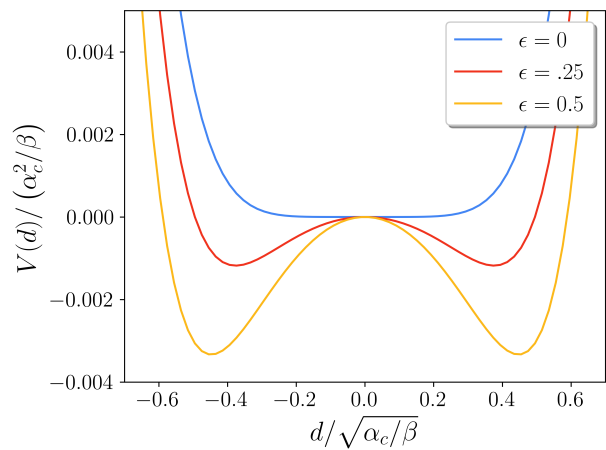


Figure 5. The potential $V(d)$ of Eq. (26) with the two minima corresponding to symmetry breaking steady states of the driven systems. The system undergoes a continuous symmetry breaking transition when driven above the threshold value $h_c = 2\gamma/\omega_1$, i.e. when $\epsilon = h/h_c - 1 > 0$.

2. Transition in the strongly damped case

Next, we address the case where h is only slightly above the instability threshold $h_c = 2\gamma/\omega_1$. Expanding Eqs. (22) in $\epsilon = (h - h_c)/h_c$ (see Supplementary Information), we find that $a(t) \approx -b(t)$ and the time dependence of the mode amplitudes is – to first order in ϵ – captured by the equation $\dot{d} = -\partial V(d)/\partial d$, where $d = a - b$ and the potential $V(d)$ is given by

$$V(d) = -\epsilon \frac{\alpha_c}{2} d^2 + \frac{\beta^2}{48\alpha_c} d^6. \quad (26)$$

The equation for \dot{d} describes a gradient descent dynamics towards one of the two minima of the potential (26). We plot the effective potential for different values of ϵ in Fig. 5 and conclude that the transition into the symmetry breaking state is continuous, i.e., the system goes through a soft bifurcation when h reaches the critical driving strength h_c . In terms of the original a and b , the potential minima [and approximate fixed points of Eqs. (22)] are located at

$$a = -b = \pm \sqrt{\frac{\alpha_c}{\beta}} (\epsilon/2)^{1/4}. \quad (27)$$

3. Crystallization in 2D

After studying plasmon pattern formation in 1D, we extend our results to two dimensions, focusing on the driving strength slightly above the instability threshold. In two dimensions, the condition $2\omega_1 = \omega_{\text{pl}}(q) + \omega_{\text{pl}}(-q)$ for selecting modes that contribute to the steady-state solution does not specify a finite set of modes. Instead, all

modes with wavevectors \mathbf{q}^* that satisfy $|\mathbf{q}^*| = q^*$ can, in principle, contribute. Studies of pattern formation in Faraday waves [88–90] suggest that a finite number of modes N with wavevectors \mathbf{q}_i^* will be selected, such that the angle between the wavevectors is given by π/N . While for $N = 1$, one obtains a standing wave, the $N = 2$ case corresponds to a square tiling and the $N = 3$ case gives a hexagonal or triangular tiling. To find the plasmon pattern to which the system converges in the steady state, we performed numerical simulations of Eqs. (7)-(8) under MFPD (for details we refer to the Supplementary Information). As closest feasible approximation to an infinite plane, we choose a periodic domain with side length commensurate with the plasmon wavelength $\lambda^* = 2\pi/q^*$. Curiously, the patterns quickly reach states with complex, quasiperiodic patterns of waves with wavelengths λ^* , then slowly settle on a nearly square pattern after a series of transformations. A typical crystallization process is shown in Fig. 6.

We find that, generally, plasmons arrange themselves in square patterns in the steady state. This is even true for square domains incommensurate with λ^* . We note that the observed patterns are not perfect square tilings. This is due to the presence of small amplitude modes with larger wavenumbers caused by the nonlinearities (see Supplementary Information). By fine tuning the boundary conditions, we were also able to realize a triangular pattern (see Supplementary Information). We also note that, under experimental conditions, noise can influence the steady state to which the system finally settles [94]. Our conclusion is that while a square tiling is preferred generally, boundary conditions can affect the final pattern.

G. Goldstone-like phonons

The crystalline steady state breaks the translational symmetry of the system. We show here that this breaking of a continuous symmetry manifests itself in the presence of Goldstone-like phonon modes. We focus on the strip geometry.

Above, we found the steady state solution: $\delta\rho = \pm\sqrt{\alpha/\beta}\sin(\omega_1 t)\cos(q^*x)$ [see Eqs. (21) and (25)] for the weakly damped case, which we will consider in this section. This solution remains valid if we shift the phase of the spatial part by ϕ :

$$\delta\rho = \pm\sqrt{\frac{\alpha}{\beta}}\sin(\omega_1 t)\cos(q^*x + \phi). \quad (28)$$

If homogeneous and static, the phase shift can always be eliminated by the coordinate transformation $x \rightarrow x - \phi/q^*$. However, if the phase shift is spatially dependent, Eq. (11) determines its dynamics. Thus, we investigate the dynamics of $\phi(t, x)$, via the ansatz $\delta\rho = \pm\sqrt{\alpha/\beta}\sin(\omega_1 t)\cos[q^*x + \phi(t, x)]$, which remains an approximate solution to Eq. (11). Since a uniform ϕ

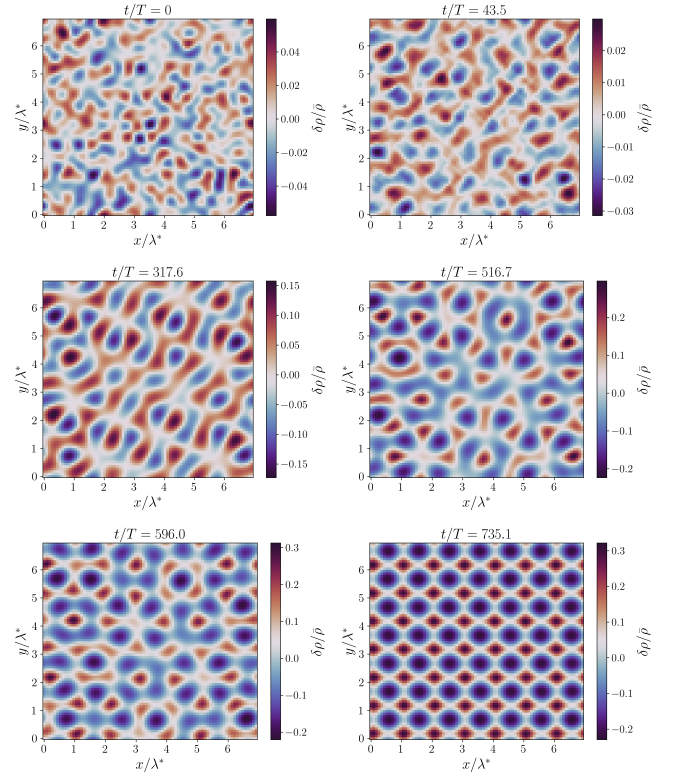


Figure 6. Plasmonic pattern formation under MFPD in two dimensions in the strongly damped regime. The plots show a numerical solution of Eqs. (7)-(10). Commensurate periodic boundary conditions were used in both directions. The driving and damping parameters used in this plot are $h = 0.05$, $\gamma = 0.045\omega_1$. An initial patterns with a characteristic periodicity of $\lambda^* = 2\pi/q^*$ forms quickly from the random initial conditions. The final stable square pattern is reached after a series of transformations. Time is given in units of $T = \pi/\omega_1$.

has no influence on the dynamics of the system, we expect slow dynamics for a long wavelength spatial dependence of $\phi(t, x)$, i.e., we expect Goldstone-like modes.

In Sec. IV C we find that the dynamics of $\phi(t, x)$ is governed by a wave equation that, to linear order, is solved by plane waves $\phi(t, x) = \text{Re}[e^{-i\Omega_{\pm}(Q)t+iQx}]$ with the dispersion:

$$\Omega_{\pm}(Q) \approx \pm\frac{\omega_1}{q^*}\sqrt{(1+3h)Q^2}. \quad (29)$$

We note that similar modes have been observed experimentally in parametrically driven classical liquids [96]. Interestingly, the dispersion (29) is linear, unlike the plasmon dispersion $\omega_{\text{pl}}(q)$. On long scales, the lattice distortions are net-neutral, therefore lacking a long-range restoring force.

1. Optical modes

Besides the Goldstone modes, the symmetry breaking state supports optical modes. These correspond to oscillations of the amplitudes a , b in Eq. (22).

To derive the dispersion of the optical modes, we expand the effective Hamiltonian in Eq. (24) around the minimum at $a = 0$, $b = \sqrt{\alpha/\beta}$:

$$H \approx -\frac{\alpha^2}{4\beta} + \alpha(\delta b^2 + \delta a^2). \quad (30)$$

The corresponding Hamilton's equations read

$$\begin{aligned} \dot{\delta b} &= 2\alpha\delta a \\ \delta \dot{a} &= -2\alpha\delta b, \end{aligned} \quad (31)$$

and are solved by a uniform oscillation of the amplitudes with the frequency 2α :

$$\delta \ddot{a} + 4\alpha^2 \delta a = 0, \quad (32)$$

with $\alpha = \omega_1 \hbar/4$.

The collective modes of the symmetry broken state described by Eqs. (29) and (32) are one possible experimental signature of the crystalline state. When the dissipation rate γ is included, the modes will obtain a negative imaginary part $\sim -i\gamma$, broadening the resonances.

H. Heating and Landau damping

Coherent driving of interacting systems leads to heating [55–69]. This can be a problem, as high temperatures can interfere with the studied effects, or even damage the systems. As described above, MFDP operates in a regime where two major sources for heating in Floquet engineered systems – radiative recombination and momentum conserving single photon absorption [23, 65] – are suppressed by the Pauli exclusion principle. Here we investigate heating due to other relevant processes, in particular disorder and phonon assisted single-photon absorption and interaction-assisted single-photon absorption.

In the first process, a single electron absorbs the energy $\hbar\Omega_F$ and is scattered by a phonon, a defect, or an impurity. In our theory, the rate of momentum relaxation is given by γ (see Eq. (8)), which captures a variety of momentum-relaxing microscopic processes. We use γ , which is related to the quality factor \mathcal{Q} , to estimate the rate of momentum non-conserving photon absorption. In the second process, the energy of a photon is distributed between two interacting electrons. This latter process is strongly suppressed by the available phase-space, constrained by energy-momentum conservation. The derivation of our estimates can be found in the Supplementary Information.

The constant influx of energy due to these two processes heats up the electrons. However, this influx is balanced by the cooling power of the cold crystal lattice. A steady state is established at an effective electron temperature T_e , where the cooling power is strong enough to fully balance the drive-induced heating. The mechanism is dominated by acoustic phonons and is well studied both experimentally [97–99] and theoretically [100] for graphene. The cooling power per electron P_{cool} is given by

$$P_{\text{cool}} = \frac{\Sigma(\bar{\rho})}{\bar{\rho}} (T_e^4 - T_{\text{ph}}^4), \quad (33)$$

where the constant $\Sigma(\bar{\rho})/\bar{\rho}$ plays the role of a material dependent coupling. For a conservative estimate, we use the values reported for graphene (see e.g. [99]). Theory shows that the cooling power in TMDs is even higher [101], such that the effective electron temperature in TMDs will be lower. We find $\Sigma(\bar{\rho}) \approx 1 \frac{\text{mW}}{\text{K}^4 \text{m}^2}$ for $\bar{\rho} \approx 10^{11} \text{cm}^{-2} - 10^{12} \text{cm}^{-2}$, $T_{\text{ph}} = 4.2 \text{K}$. A detailed estimation of the rates of photon absorption (see Supplementary Information) gives a heating power of $P_{\text{drive}} = 2.7 \cdot 10^6 \text{eV/s}$, for the driving strength required to reach the instability threshold (see Discussion section). Equating $P_{\text{cool}} = P_{\text{drive}}$, we find an effective electron temperature of $T_e \approx 20 \text{K}$. This is well below the typical temperatures in plasmonics experiments [80]. Moreover, due to the nonlinear dependence of the cooling power P_{cool} on the electron temperature, increasing the driving power by two orders of magnitude would result in an effective electron temperature of only $T_e \approx 60 \text{K}$.

All in all, we find that driving induced heating is controlled in the setting we propose. Most importantly, we find that the driving induced heating is too weak to significantly increase the Landau damping of plasmons, which is strongly suppressed by the \sqrt{q} -shape of the plasmon dispersion, lying – for the frequencies considered here – outside the particle-hole continuum [102].

III. DISCUSSION

Gapped two dimensional Dirac materials are currently an active area of research in material science [103, 104] and promising candidates for Floquet engineering. Recently, ARPES measurements revealed light-induced gaps in black phosphorus [16] and Floquet-Bloch states in graphene [105, 106] in the off-resonant regime considered here. Many interesting features of MFDP, such as the enhancement of plasmon quality factors, as well as exceptional points and non-dispersive states, appear below the critical driving strengths determined by the instability condition $\hbar > 2\gamma/\omega_1$, making them accessible for lasers with relatively low powers. To estimate the power necessary to induce the non-equilibrium crystalline phase, we assume typical values for the parameters of our system: $E_g = 0.3 \text{eV}$, $\hbar\Omega_F = 0.35 \text{eV}$, $\lambda = 15 \text{eV}\text{\AA}$. Assuming an electron density of $\bar{\rho} = 1.18 \cdot 10^{11} / \text{cm}^{-2}$,

such that the chemical potential is close to, but above the resonance, and a plasmon quality factor of $\mathcal{Q} = \omega_1/\gamma \approx 10^2$, from the instability condition $h > 2\gamma/\omega_1$, we find the necessary critical amplitude of the electric field to be $\bar{\mathcal{E}} \approx 4 \cdot 10^5$ V/m with a modulation amplitude $\delta\bar{\mathcal{E}} = 0.5\bar{\mathcal{E}}$. Thus the laser intensity required to induce the transition to the crystalline state is by a factor of 10^4 smaller than in current solid state Floquet engineering experiments [12–14, 16] and generally within the reach of continuous wave lasers. The critical driving strength is essentially determined by the plasmon \mathcal{Q} . While quality factors of $\mathcal{Q} \approx 1.5 \cdot 10^2$ have been observed in graphene [80], quality factors of up to $10^3 - 10^4$ are believed to be reachable in principle [80, 81]. Such high quality factors would allow to further reduce the necessary laser intensity. On the other hand, as shown in Sec. IIH, the suppression of heating in the off-resonant regime used by MFPD allows, in principle, to increase the driving power by at least two orders of magnitude. Thus, MFPD may be even achievable with low quality plasmons, if sufficiently strong drives are used.

The phenomena presented here can be implemented in two dimensional Dirac systems, such as black phosphorus or TMDs [107]. Another candidate for realizing our ideas is graphene, where Floquet-Bloch states have also been observed at different driving energies [14, 105, 106].

In summary, modulated Floquet parametric driving offers a road to realize new non-equilibrium electron phases with broken translation symmetries in time and space and non-trivial Goldstone modes. Additionally, MFPD opens new possibilities to excite and control THz plasmons by optical or infrared signals. Given the interest in efficient THz technology, the realization of plasmonic parametric amplifiers, time reversal mirrors and other effects predicted for time-varying photonic materials [82, 83, 108] will advance current research on plasmons. A direct observation of exceptional points and non-dispersive regions can be achieved by mapping the plasmon dispersion, e.g., with spectroscopic measurements [109], while the crystalline plasmon phase can be detected via scanning near-field optical microscopy which can be used to measure the periodic density $\delta\rho$ of the crystalline state [110, 111]. The plasmon lattice could also be observed through light or electron scattering experiments, where it would act similarly to a 2D grating. Finally, we note that similar physics could be implemented using other types of collective modes, e.g., magnons.

IV. METHODS

A. Slowly varying envelope approximation

To find the exceptional points and instabilities of plasmon waves under MFPD (see Sec. IID), we solve Eq. (12) in the vicinity of the resonance $\omega_{\text{pl}}(q) = \omega_1$ with the

slowly varying envelope approximation [76]. The ansatz

$$\delta\rho_q = a_q(t) \cos(\omega_1 t) + b_q(t) \sin(\omega_1 t), \quad (34)$$

when used in Eq. (12), leads to the two equations

$$\begin{aligned} -\frac{1}{2}\omega_1^2 h b_q - 2\dot{a}_q \omega_1 - \gamma a_q \omega_1 + (\omega_{\text{pl}}^2(q) - \omega_1^2) b_q &= 0 \\ \frac{1}{2}\omega_1^2 h a_q + 2\dot{b}_q \omega_1 + \gamma b_q \omega_1 + (\omega_{\text{pl}}^2(q) - \omega_1^2) a_q &= 0, \end{aligned} \quad (35)$$

where we neglected the second derivatives of a_q and b_q , as they are of higher order in the small h around $\omega_{\text{pl}}(q) = \omega_1$. Assuming $a = a(0) e^{s(q)t}$, $b = b(0) e^{s(q)t}$, leads to Eq. (15).

B. Analysis of nonlinear pattern formation

In this section we derive the results on the plasmon crystallization presented in Sec. IIF. We first study the strip geometry where the y -axis is confined to a width l with $l < 2\pi/q^*$. In this quasi-1D geometry, we have to replace the Fourier transform of the Coulomb potential $V(q)$ in Eq. (13) by

$$V(q) \approx \int_0^l dy \int_{-\infty}^{\infty} dx \frac{e^{i\mathbf{q}\cdot\mathbf{x}}}{|\mathbf{x}|} \approx 2l \left| \ln \frac{|q|l}{4} \right|. \quad (36)$$

As pointed out in Sec. IIF, for the analysis of pattern formation caused by parametric instabilities, it is sufficient to consider a projection of Eq. (8) on the subset of linearly unstable modes of Eq. (34) [86, 88]. This excludes second order nonlinearities. These give rise to frequency doubling modes which lie outside of the considered subspace. The third order terms, however, contribute to oscillations at the base frequency ω_1 . Keeping in mind that $\mathbf{u} \propto \mathbf{q}^*$ for plasmons, we use the linearized continuity equation $\delta\dot{\rho} = -\bar{\rho}\nabla\mathbf{u}$ to approximate

$$u_{s,i} \approx -\partial_i \frac{\delta\dot{\rho}_s}{q^* 2\bar{\rho}}. \quad (37)$$

At this point, it is useful to simplify Eq. (11). Rescaling $\delta\rho_s = h^{1/2}\delta\tilde{\rho}_s$, we find that to order $\mathcal{O}(h)$, the time dependence of m^* in front of the nonlinear terms can be neglected for $h \ll 1$. With the approximations described above, for the purpose of finding the modulated pattern of the steady state, Eq. (11) is reduced to

$$\begin{aligned} \partial_t m^*(t) \partial_t \delta\rho_s + \gamma \bar{m}^* \partial_t \delta\rho_s + \bar{m}^* \omega_1^2 \delta\rho_s \\ - \frac{\bar{m}^*}{q^* 4 \bar{\rho}^2} \partial_i \partial_j \delta\rho_s (\partial_i \delta\dot{\rho}_s) (\partial_j \delta\dot{\rho}_s) = 0, \end{aligned} \quad (38)$$

where $\delta\rho_s$ is given by Eq. (21). Derivatives (except those in parenthesis) act on all functions to their right. An evaluation of Eq. (38) in which modes lying outside the subspace of linearly unstable modes are neglected leads to Eq. (22), which is the nonlinear generalization of the slowly varying mode approximation of Eq. (35).

C. Deriving the Goldstone modes

Here, we derive the dispersions of the Goldstone-like modes in the symmetry breaking steady state. Starting from Eq. (28), we write

$$\delta\rho = \frac{1}{2}\sqrt{\frac{\alpha}{\beta}} [\sin(\omega_1 t - q^* x - \phi(t, x)) + \sin(\omega_1 t + q^* x + \phi(t, x))], \quad (39)$$

and choose the ansatz

$$\phi(t, x) = \text{Re}\phi_0 e^{-i\Omega t + iQ \cdot x} \quad (40)$$

for $\phi(t, x)$, where

$$\frac{Q}{q^*} \ll 1, \quad \frac{\Omega}{\omega_1} \ll 1. \quad (41)$$

We insert Eq. (39) into Eq. (11) and compare the coefficients in front of the resulting $\sin[\omega_1 t \pm q^* x \pm \phi(t, x)]$ and $\cos[\omega_1 t \pm q^* x \pm \phi(t, x)]$ terms in the equations. The equation governing the propagation of the local phase shift $\phi(t, x)$ follows from the cosine terms. To leading order in $\varphi(t, x)$, Q/q_s and Ω/ω_1 , we find

$$\frac{\partial^2}{\partial t^2} \phi = \frac{\omega_1^2/q^{*2}}{1 - h/2} \left(1 + \frac{5}{2}h\right) \frac{\partial^2}{\partial x^2} \phi. \quad (42)$$

The wave equation (42) leads to the dispersion of Goldstone-like phonons (29) in Sec. II G. The equation obtained from comparing the coefficients in front of the sine terms is fulfilled identically to leading order in Ω/ω_1 . A more detailed version of this derivation can be found in the Supplementary Information.

ACKNOWLEDGMENTS

We acknowledge useful conversations with Dmitri Basov, Gaurav K. Gupta, Amit Kanigel, and Yiming Pan. E.K. and N.L. thank the Helen Diller Quantum Center for financial support. N.L. is grateful for funding from the ISF Quantum Science and Technology (2074/19) and from the Defense Advanced Research Projects Agency through the DRINQS program, grant No. D18AC00025. M. R. is grateful to the University of Washington College of Arts and Sciences and the Kenneth K. Young Memorial Professorship for support.

SUPPLEMENTARY INFORMATION

A. Enhancing plasmonic quality factors with MFPD

Here we show, how MFPD below the instability threshold can be used to enhance plasmon quality factors. Adding a forcing of the form $f = \cos(\omega_1 t) \delta(q_y)$ to the right hand side of Eq. (12), we find

$$\partial_t (1 + h \cos(2\omega_1 t)) \partial_t \delta \rho_q + \gamma \partial_t \delta \rho_q + \omega_{\text{pl}}^2(q) \delta \rho_q = f \cos(\omega_1 t) \delta(q_y). \quad (\text{S1})$$

For simplicity, we assumed that the forcing is uniform along the y -direction and pointlike on the x -axis. In real space, we have $f = \cos(\omega_1 t) \delta(x)$. This forcing will induce plasmons at $x = 0$, which will then propagate along the x -direction.

Modifying the amplitude equations (35) to include the forcing term, and setting the derivatives \dot{a}_q, \dot{b}_q to zero (we are looking for the steady-state solutions) we find:

$$\begin{aligned} -\frac{1}{2}\omega_1^2 h b_q - \gamma a_q \omega_1 + (\omega_{\text{pl}}^2(q) - \omega_1^2) b_q &= f \\ \frac{1}{2}\omega_1^2 h a_q + \gamma b_q \omega_1 + (\omega_{\text{pl}}^2(q) - \omega_1^2) a_q &= 0. \end{aligned}$$

Solving for a_q we find

$$\begin{aligned} a_q &= \frac{\gamma \omega_1 f}{\left(\frac{\omega_1^2 h}{2}\right)^2 - (\omega_{\text{pl}}^2(q) - \omega_1^2)^2 - (\gamma \omega_1)^2} \\ b_q &= -\frac{1}{\gamma \omega_1} \left[\frac{1}{2} \omega_1^2 h + (\omega_{\text{pl}}^2(q) - \omega_1^2) \right] a_q \sim -\frac{\omega_1 h}{\gamma} a_q \end{aligned}$$

For brevity, we write

$$\omega_{\text{pl}}^2 = 2Aq$$

with

$$A = \frac{2\pi e^2 \bar{\rho}}{\varepsilon \bar{m}^*}.$$

For the resulting plasmon wave, we find

$$\begin{aligned} a(x) &= \int_{-\infty}^{\infty} dq \frac{\gamma \omega_1 f e^{iqx}}{\left(\frac{\omega_1^2 h}{2}\right)^2 - (2Aq - \omega_1^2)^2 - (\gamma \omega_1)^2} \\ &= -e^{iq^* x} \frac{\gamma e^{-q^* \sqrt{\gamma^2/\omega_1^2 - h^2/4}|x|}}{2A \sqrt{4\gamma^2 - h^2\omega_1^2}}. \end{aligned}$$

Setting $h = 0$ for a moment, we recognize that the damping γ results in an exponential decay of the plasmon wave along the x -axis due to the factor $e^{-\frac{q^*}{\mathcal{Q}}|x|}$, where $\mathcal{Q} = \omega_1/\gamma$ is the quality factor. MFPD below the instability threshold $h = 2\gamma/\omega_1$ results in an enhanced plasmon quality factor

$$\mathcal{Q}(h) = \frac{1}{\sqrt{\gamma^2/\omega_1^2 - h^2/4}} \quad (\text{S2})$$

$$= \frac{\mathcal{Q}}{\sqrt{1 - h^2 \mathcal{Q}^2/4}} \quad (\text{S3})$$

and thereby in a longer propagation length. The enhancement effect on the plasmon amplitude is exponential, such that even a small improvement of \mathcal{Q} will result in a strongly increased amplitude of the plasmon field far away from the source. E.g. for the parameters $\gamma = 0.1\omega_1$, i.e., $\mathcal{Q} = 10$ and a driving $h = \gamma/\omega_1$, which is half the driving amplitude

required to reach the instability threshold, from Eq. (S2), we expect an effective quality factor of $\mathcal{Q}(h) \approx 11.5$. As $h \rightarrow 2\gamma/\omega_1$, we find $\mathcal{Q} \rightarrow \infty$. By approaching the instability threshold, the quality of plasmon resonances can be increased to very high values.

To support our findings, we solved for the plasmon dynamics numerically. We first simplify the equations of motion. Starting with Eq. (S1), and anticipating that the amplitude variation of the plasmon wave along the x -direction will be slow, i.e., the width of the plasmon wave-packet along the q_x -axis will be small, we expand $\omega_{\text{pl}}^2(q_x)$ around the resonant q^* . We find $\omega_{\text{pl}}(q^* + \Delta q) \approx 2Aq_x^* + 2A\Delta q_x$. Next, we approximate this dispersion with the dispersion of a massive wave equation $\omega_{\text{m}}^2(q_x) = m^2 + Bq_x^2$. Equating $\omega_{\text{m}}^2(q^* + \Delta q_x) = \omega_{\text{pl}}^2(q^* + \Delta q)$ to first order in Δq_x , gives $m^2 = Aq^*$, $B = A/q^*$. Thus for wavepackets centered narrowly around q^* , in real space, Eq. (S1) can be approximated with the massive wave equation

$$\partial_t [1 + h \cos(2\omega_1 t)] \partial_t \delta\rho(x) + \gamma \partial_t \delta\rho(x) + \left(Aq^* - \frac{A}{q^*} \partial_x^2 \right) \delta\rho_q = f \cos(\omega_1 t) \delta(x).$$

Furthermore, it is easy to see by inserting the ansatz of Eq. (34), that to first order in h , we can approximate

$$\partial_t (1 + h \cos(2\omega_1 t)) \partial_t \delta\rho(x) \approx (1 - h \cos(2\omega_1 t)) \partial_t^2 \delta\rho(x), \quad (\text{S4})$$

since both expressions lead to the same amplitude equations (34). Thus, dividing by $(1 - h \cos(2\omega_1 t))$, to leading order in $h \ll 1$, the approximate wave equation for plasmon propagation reads

$$\partial_t^2 \delta\rho(x) + \gamma \partial_t \delta\rho(x) + (1 + h \cos(2\omega_1 t)) \left(Aq^* - \frac{A}{q^*} \partial_x^2 \right) \delta\rho_q = f \cos(\omega_1 t) \delta(x).$$

We use the Dedalus spectral solver [85] to solve this PDE. We find that our numerical results agree very well with the prediction of Eq. (S2) (see main text).

B. Plasmonic pattern formation

1. ϵ -expansion of the amplitude equations

To derive the gradient descent dynamics of the amplitudes towards the steady state characterized by the minima of Eq. (26) of the main text, we write Eqs. (22) of the main text in terms of transformed variables $c = a + b$ and $d = a - b$:

$$\begin{aligned} \dot{c} &= -\frac{\gamma}{2}c - \alpha c + \frac{\beta}{2}d(c^2 + d^2) \\ \dot{d} &= -\frac{\gamma}{2}d + \alpha d - \frac{\beta}{2}c(c^2 + d^2). \end{aligned} \quad (\text{S5})$$

Introducing the small parameter $\epsilon = (h - h_c)/h_c$, and writing $\alpha_c = \omega_1 h_c/4$, we find

$$\begin{aligned} \dot{c} &= -\alpha_c(2 + \epsilon)c + \frac{\beta}{2}d(c^2 + d^2) \\ \dot{d} &= \alpha_c \epsilon d - \frac{\beta}{2}c(c^2 + d^2). \end{aligned} \quad (\text{S6})$$

The small ϵ defines a slow time scale connected to the growth of the unstable modes. Next, we expand in terms of ϵ and write $c = \epsilon^{1/4}c_1 + \epsilon^{3/4}c_2 + \dots$, $d = \epsilon^{1/4}d_1 + \epsilon^{3/4}d_2 + \dots$ and $\partial_t = \partial_{t_0} + \epsilon \partial_{t_1} + \dots$. At orders $\epsilon^{1/4}$ and $\epsilon^{3/4}$, we find

$$\begin{aligned} \frac{\partial c_1}{\partial t_0} &= -2\alpha_c c_1 \\ \frac{\partial c_2}{\partial t_0} &= -2\alpha_c c_2 + \frac{\beta}{2}d_1(c_1^2 + d_1^2). \end{aligned}$$

These equations describe a quick (order ϵ^0) relaxation towards the fixed point

$$\begin{aligned} c_1 &= 0 \\ c_2 &= \frac{\beta}{4\alpha_c} d_1^3. \end{aligned} \quad (\text{S7})$$

At order $\epsilon^{5/4}$ we find corrections to this dynamics, which describe how the system settles into the symmetry breaking fixed point after \bar{a} has taken the value given by Eq. (S7). In particular, we find

$$\frac{\partial d_1}{\partial t_1} = \alpha_c d_1 - \frac{\beta}{2} c_2 d_1^2.$$

Since the relaxation of c_2 towards the value given by Eq. (S7) is fast, we can write

$$\frac{\partial d_1}{\partial t_1} = \alpha_c d_1 - \frac{\beta^2}{8\alpha_c} d_1^5. \quad (\text{S8})$$

In terms of the original variables t and \bar{b} the above equation reads:

$$\frac{\partial d}{\partial t} = \epsilon \tilde{h}_c \omega_1 d - \frac{\beta^2}{8\alpha_c} d^5. \quad (\text{S9})$$

This equation can be written as

$$\frac{\partial d}{\partial t} = -\frac{\partial V(d)}{\partial d},$$

with the potential $V(d)$ given by Eq. (26) of the main text.

2. 2D Plasmonic patterns in the symmetry breaking phase

Whereas for the strip geometry the only feasible pattern for the crystalline phase is a standing wave, for the 2D plane a variety of patterns is possible. We investigated the pattern formation using the approach of Refs. [88, 90], which analyzed pattern formation for Faraday waves. For the 2D setting we modify the ansatz of Eq. (21) to

$$\begin{aligned} \delta\rho_s(t, \mathbf{x}) = & \cos(\omega_1 t) \sum_{i=1}^N a^{(i)}(t) \cos(\mathbf{q}^{*(i)} \cdot \mathbf{x}) \\ & + \sin(\omega_1 t) \sum_{i=1}^N b^{(i)}(t) \cos(\mathbf{q}^{*(i)} \cdot \mathbf{x}). \end{aligned} \quad (\text{S10})$$

with

$$|\mathbf{q}^{*(i)}| = q^*. \quad (\text{S11})$$

The nonlinearity of the system determines the ordering pattern, which is reflected in the number of wavevectors N in Eq. (S10) and their respective angles [88–90]. Typically a roll ($N = 1$), a square lattice ($N = 2$) or a hexagonal lattice ($N = 3$) is formed, depending on the parameters of the system. The angles between the \mathbf{q}_i^* are $\pi/2$ for the $N = 2$ and $\pi/3$ for the $N = 3$ case (we note that this reasonable assumption can fail in certain cases, e.g., for non-trivial domain boundaries).

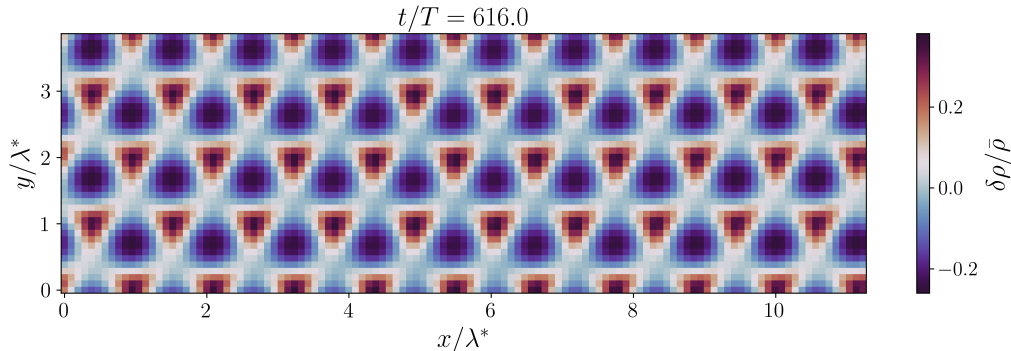
Inserting the ansatz (S10) into Eq. (38), we derive equations of motion analogous to those of Eq. (22). In equilibrium the system is rotationally symmetric, and we assume that all standing waves in Eq. (21) have equal amplitudes: $a^{(i)} = a$, $b^{(i)} = b$, for all i . This is a common assumption in the analysis of pattern formation due to parametric instabilities [88, 90]. The amplitude equations read

$$\begin{aligned} \dot{a} &= -\alpha b - \frac{1}{2}\gamma a + \beta_N b (a^2 + b^2) \\ \dot{b} &= -\alpha a - \frac{1}{2}\gamma b - \beta_N a (a^2 + b^2) \end{aligned}$$

and are identical with Eqs. (22), except that the coefficient $\beta \rightarrow \beta_N$ now depends on the number of modes considered. Specifically, we find

$$\beta_1 = 2\omega_1/32(\bar{\rho})^2 \quad (\text{S12})$$

$$\beta_{N>1} = (2N - 2)\omega_1/32(\bar{\rho})^2, \quad (\text{S13})$$



Supplementary Figure S 1. Triangular pattern observed for a sample with boundary lengths $11.32\lambda^*$ and $3.91\lambda^*$.

where the angle between neighboring $\mathbf{q}^{*(i)}$ was assumed to be π/N , giving equal angles between all $\mathbf{q}^{*(i)}$. In the main text [see Eq. (26)], we found that for a slightly supercritical driving, the system settles in the minimum of the potential function

$$V(d) = -\epsilon \frac{\alpha_c}{2} d^2 + \frac{\beta_N^2}{48\alpha_c} d^6$$

when the initial growth is saturated. Here, $d = a - b$. Since the value of $V(\bar{b})$ at the two minima scales as β_N^{-1} , we conclude that the larger the number of modes N , the more shallow the minima. However, from Eqs. (S12), (S13) follows, that the minima corresponding to standing waves ($N = 1$) and square patterns ($N = 2$) have the same depth. To settle the question which pattern will be chosen, we have to go beyond our approximation.

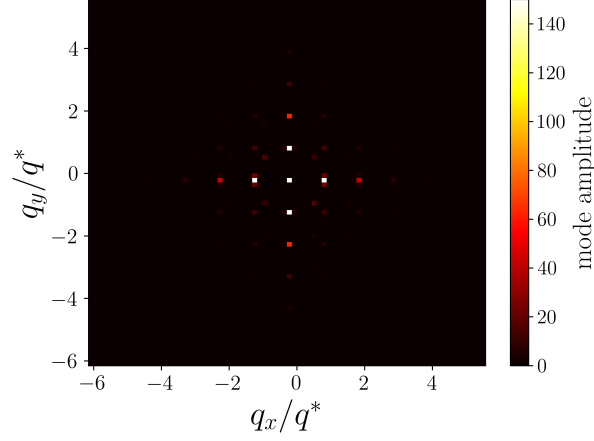
Our aim is to show that symmetry breaking and pattern formation will occur in general, and to predict the most probable patterns. To this aim, we use numerical simulations and leave a more involved analytical treatment for future work. We again use the Dedalus spectral solver [85] and solve equations (7)-(10) numerically, applying the approximation of Eq. (S4). This approximation is necessary, as Dedalus does not allow to combine time varying terms and time derivatives. The 2D Coulomb operator was implemented in its Fourier representation $V(q) = 2\pi/q$.

For the simulations we used the parameters $h = 0.05$, $\gamma = 0.0249\omega_1$. We are thus in the strongly damped regime with $\epsilon = (h - h_c)/h_c \approx 0.004$. We used a square domain with side length of $7\lambda^*$, where $\lambda^* = 2\pi/q^*$ is the wavelength of the unstable modes, and applied periodic boundary conditions. A larger domain would have significantly increased the computational time. In all 10 runs of our simulation the plasmons arranged themselves in square patterns. We conclude that this is the generic steady state for a clean system. Fig. 6 of the main text shows the formation of the square pattern starting from a smooth, random charge distribution.

Choosing incommensurate boundary length and different aspect ratios, we found that the waves converge to a square pattern in most cases. The pattern was mostly rotated with respect to the domain boundaries to accommodate the periodicity of the pattern. For some aspect ratios, the tiling was distorted, and the angle between the two modes \mathbf{q}_1^* , \mathbf{q}_2^* was less than 90 degrees. For a sample with boundary length $11.32\lambda^*$ and $3.91\lambda^*$ a nearly triangular pattern was observed (Fig. S 1). However, we could not repeat this result with other aspect ratios, and conclude that it is the effect of fine-tuned boundary conditions.

3. Harmonics and deviations from the square pattern

As mentioned in the main text, the observed patterns are not perfect square tilings. This is due to the presence of harmonics which result in wavemodes with wavenumbers $q = 2q^*$ (see Fig. which shows the Fourier spectrum of the last pattern in Fig. 6 of the main text). The origins of these modes lie beyond our analytic treatment, however, they are clearly subleading with respect to the main modes of the square tiling. We note that there are also very weak contributions with wavenumbers on the order of $q \sim \sqrt{2}q^*$.



Supplementary Figure S 2. Fourier spectrum of the final pattern in Fig. 6 of the main text. While the leading modes are those corresponding to the square tiling and wavevectors of length q^* (closest to the center), the spectrum is enriched by modes with wavenumbers $2q^*$.

C. Goldstone-like phonons

It is useful to rewrite the solution in Eq. (28) as the sum of two moving waves

$$\delta\rho_\varphi = \frac{\sqrt{\alpha/\beta}}{2} [\sin(\omega_1 t - q^* x - \varphi(t, x)) + \sin(\omega_1 t + q^* x + \varphi(t, x))]. \quad (\text{S } 14)$$

To be concise, in what follows, we will abbreviate

$$\begin{aligned} \sin(\omega_1 t - qx - \varphi(t, x)) &= \sin(-) \\ \sin(\omega_1 t + qx + \varphi(t, x)) &= \sin(+), \end{aligned}$$

and similarly for the cosines. For $\varphi(t, x)$, we choose the ansatz

$$\varphi(t, x) = \text{Re}\varphi_0 e^{-i\Omega t + iQ \cdot x}. \quad (\text{S } 15)$$

A weak spatial dependence of $\varphi(t, x)$ means

$$\frac{Q}{q^*} \ll 1. \quad (\text{S } 16)$$

Furthermore, we expect soft modes, such that

$$\frac{\Omega}{\omega_1} \ll 1. \quad (\text{S } 17)$$

Eqs. (S 16) and (S 17) significantly simplify the calculations.

We first study the action of the Coulomb kernel on the Goldstone mode φ . Linearizing $\delta\rho$ in φ gives

$$\delta\rho_\varphi \approx \sqrt{\frac{\alpha}{\beta}} \sin(\omega_1 t) [\cos(q^* \cdot x) - \sin(q^* \cdot x) \varphi(\mathbf{x}, t)].$$

We have linearized in φ , and it is more convenient to use the complex plain wave ansatz $\varphi(t, x) = \varphi_0 e^{-i\Omega t + iQ \cdot x}$. Inserting the above expression into the Coulomb integral, we find

$$\int d^2 x' \frac{\cos(\mathbf{q}^* \cdot \mathbf{x})}{|\mathbf{x} - \mathbf{x}'|} = V(q^*) \cos(\mathbf{q}^* \cdot \mathbf{x})$$

and

$$\begin{aligned} \int d^2 x' \frac{\sin(\mathbf{q}^* \cdot x) \varphi(\mathbf{x}, t)}{|\mathbf{x} - \mathbf{x}'|} &\approx \frac{\varphi_0}{2i} e^{-i\Omega t} \left(V(|\mathbf{q}^* + \mathbf{Q}|) e^{i(\mathbf{q}^* + \mathbf{Q}) \cdot \mathbf{x}} - V(|\mathbf{q}^* - \mathbf{Q}|) e^{-i(\mathbf{q}^* - \mathbf{Q}) \cdot \mathbf{x}} \right) \\ &\approx V(q^*) \sin(\mathbf{q}^* \cdot \mathbf{x}) \varphi(\mathbf{x}, t) + \frac{1}{i} \frac{\partial V(q)}{\partial \mathbf{q}} \cdot \mathbf{Q} \cos(\mathbf{q}^* \cdot \mathbf{x}) \varphi(\mathbf{x}, t). \end{aligned} \quad (\text{S } 18)$$

These expressions are valid both for the infinite 2d plane, where

$$V(q) = \frac{2\pi}{q},$$

and the strip geometry (with the y -axis confined to $0 < y < l$ with $l \ll 2\pi/q^*$), where

$$V(q) = 2l \left| \ln \frac{|q|l}{4} \right|$$

and $\mathbf{q} \propto \hat{\mathbf{e}}_x$. We see from Eq. (S18) that the spatial dependence of $\varphi(x, t)$ results in a small correction of the order of Q/q^* in the 2d plane case, and $Q/q^* \ln q^*$ for the strip. Ignoring this correction, we have

$$\int d^2x' \frac{\delta\rho_\varphi}{|\mathbf{x} - \mathbf{x}'|} \approx V(q^*) \delta\rho_\varphi.$$

Therefore, to linear order in ϕ , we can write Eq. (11) as [see Eqs. (37) and (38)]:

$$\partial_t (1 + h \cos(2\omega_1 t)) \partial_t \delta\rho_\varphi + \gamma \partial_t \delta\rho_\varphi - \frac{\omega_1^2}{q^{*2}} \partial_i \partial_i \delta\rho_\varphi + \frac{1}{q^{*4} \bar{\rho}^2} \partial_i \partial_j \delta\rho_\varphi (\partial_i \delta\rho_\varphi) (\partial_j \delta\rho_\varphi) = 0. \quad (\text{S19})$$

We now insert Eq. (S14) in Eq. (S19) and neglect terms oscillating at frequencies $3\omega_1$ and wavenumbers $3q^*$. Comparing the coefficients in front of the $\sin[\omega_1 t \pm q^* x \pm \varphi(t, x)]$ and $\cos[\omega_1 t \pm q^* x \pm \varphi(t, x)]$ terms, we find the equation governing the propagation of the local phase shift $\varphi(t, x)$. Notice that the equation obtained by comparing the coefficients also contains corrections of order $\mathcal{O}(\Omega/\omega_1)$ and higher orders in Ω/ω_1 to the dispersion $\omega_{\text{pl}}(q)$. These describe the back action of the propagating phase $\varphi(t, x)$ on the solution $\delta\rho_\varphi$. Terms contributing to these corrections can be easily recognized as they change sign depending on the parallel or anti-parallel orientation of Q with respect to $\pm q^*$, i.e., for the two waves $\sin[\omega_1 t \pm q^* x \pm \varphi(t, x)]$ (and similar for the cos terms). We neglect these corrections. The equation governing the dynamics of $\varphi(t, x)$ follows from the cos terms. To leading order in $\varphi(t, x)$, Q/q_s and Ω/ω_1 , we find the equation appearing in the main text:

$$\frac{\partial^2}{\partial t^2} \varphi = \frac{\omega_1^2/q^{*2}}{1 - h/2} \left(1 + \frac{5}{2}h \right) \frac{\partial^2}{\partial x^2} \varphi. \quad (\text{S20})$$

D. Heating and Landau damping

In undoped gapped systems, the main heating mechanisms are radiative recombination and momentum conserving single photon absorption [23, 65]. In the proposed set-up, these processes are suppressed by the exclusion principle. The most relevant allowed heating processes are phonon- or disorder-assisted, momentum non-conserving single-photon absorption and interaction-assisted single-photon absorption. Here we estimate the heating due to these processes and show that the Landau damping induced by this heating is very small.

In the following we calculate the number of electrons excited by momentum non-conserving single-photon absorption per unit of time and area Γ_γ , and the corresponding number for interaction-aided single-photon absorption Γ_{int} .

1. Estimation of Γ_γ

The matrix element for the absorption of n photons is proportional to $(e\mathcal{E}\lambda/\hbar\Omega_F^2)^n$ (see, e.g., [23]) and the rate of momentum non-conserving scattering is γ_{mom} . Thus, according to Fermi's Golden rule, the scattering rate can be estimated as $\gamma_{\text{mom}} (e\mathcal{E}\lambda/\hbar\Omega_F^2)^{2n}$. To find Γ_γ , we have to multiply by the density of electrons available for this kind of scattering. Slightly overestimating this density (and the heating due to this process), we approximate it by the total electron density of the upper band $\rho = \pi k_F^2 / (2\pi)^2$. We thus find

$$\Gamma_\gamma \approx \frac{\gamma_{\text{mom}} \pi k_F^2}{(2\pi)^2} \left(\frac{e\mathcal{E}\lambda}{\hbar\Omega_F^2} \right)^2. \quad (\text{S21})$$

Using the estimates from the main text ($\hbar\Omega_F = 0.35$ eV, $\lambda = 15$ eVÅ, $\bar{\mathcal{E}} \approx 4 \cdot 10^5$ V/m), the dimensionless amplitude of the electric field controlling the strength of the photon absorption is

$$\frac{e\mathcal{E}\lambda}{\hbar\Omega_F^2} \approx 5 \cdot 10^{-3}.$$

The specific value of γ_{mom} depends on sample properties and is unknown. However, for a conservative estimation we can set $\gamma_{\text{mom}} = \gamma$, where γ is the decay rate of the plasmon waves introduced in the main text. γ can be estimated using values for the plasmon quality factor Q . This is an overestimate of γ_{mom} , and hence the heating rate, since the plasmon quality is lowered by the decay of the plasmon-induced electric fields in the substrate – a process which does not contribute to γ [80]. A quality factor of $Q = \omega/\gamma = 10^2$ [80] gives $\gamma \approx 6.28 \cdot 10^{10} \text{Hz}$ for a plasmon frequency of $\omega/2\pi = 1 \text{THz}$. We thus find

$$\begin{aligned}\Gamma_\gamma &\approx 2.5 \cdot 10^{-5} \cdot \gamma \rho \\ &\approx 1.6 \cdot 10^6 \text{Hz} \cdot \rho.\end{aligned}$$

2. Estimation of Γ_{int}

In this process, a single photon is absorbed and its energy is distributed between two electrons. The two electrons exchange a momentum \mathbf{q} through Coulomb interaction. Energy conservation yields

$$\varepsilon(\mathbf{k}_1 + \mathbf{q}) + \varepsilon(\mathbf{k}_2 - \mathbf{q}) - \varepsilon(\mathbf{k}_2) - \varepsilon(\mathbf{k}_1) - \hbar\Omega_F = 0.$$

Thus, the available phase space for this process is very limited. The Coulomb potential is given by

$$V(\mathbf{q}) = \frac{e^2}{\varepsilon} \frac{2\pi}{q + q_s},$$

where the screening length is $q_s \approx 4\alpha k_F$, with the fine structure constant $\alpha = e^2/\varepsilon\lambda$ [112]. This approximation is valid when the Fermi energy is far enough from the bottom of the band and the dispersion is nearly linear. For the estimate at hand, we approximate

$$\begin{aligned}V(0) &\approx \frac{e^2}{\varepsilon} \frac{2\pi}{q_s} \\ \varepsilon(\mathbf{k}) &\approx \lambda k\end{aligned}$$

The number of absorbed photons per unit of time can then be estimated using Fermi's Golden rule as

$$\Gamma_{\text{int}} \approx \frac{1}{\hbar} \int \frac{d^2 k_1}{(2\pi)^2} \int \frac{d^2 k_2}{(2\pi)^2} \int \frac{d^2 q}{(2\pi)^2} \delta(\varepsilon(\mathbf{k}_1 + \mathbf{q}) + \varepsilon(\mathbf{k}_2 - \mathbf{q}) - \varepsilon(\mathbf{k}_2) - \varepsilon(\mathbf{k}_1) - \hbar\Omega_F) V^2(0) \left(\frac{e\mathcal{E}\lambda}{\hbar\Omega_F^2} \right)^2.$$

To take the integrals, it is useful to introduce dimensionless variables

$$\begin{aligned}\mathbf{K}_i &= \mathbf{k}_i/k_F \\ \mathbf{Q}' &= \mathbf{q}/k_F \\ \bar{\Omega} &= \hbar\Omega_F/\lambda k_F\end{aligned}$$

(Q' is not to be confused with the wavenumber of the Goldstone-like modes, Q). The above integral can then be written as

$$\Gamma_{\text{int}} = \frac{V^2(0) k_F^6}{\lambda \hbar k_F} \left(\frac{e\mathcal{E}\lambda}{\hbar\Omega_F^2} \right)^2 \int \frac{d^2 K_1}{(2\pi)^2} \int \frac{d^2 K_2}{(2\pi)^2} \int \frac{d^2 Q'}{(2\pi)^2} \delta(|\mathbf{K}_1 + \mathbf{Q}'| + |\mathbf{K}_2 - \mathbf{Q}'| - |\mathbf{K}_2| - |\mathbf{K}_1| - \bar{\Omega}).$$

The q integration can be performed by going to elliptical coordinates. This procedure (for details see e.g. [113]) yields

$$\Gamma_{\text{int}} = \frac{V^2(0) k_F^5}{\hbar\lambda} \left(\frac{e\mathcal{E}\lambda}{\hbar\Omega_F^2} \right)^2 \int \frac{d^2 K_1}{(2\pi)^2} \int \frac{d^2 K_2}{(2\pi)^2} \int \frac{d\vartheta}{(2\pi)^2} |\mathbf{K}_1 + \mathbf{K}_2| \frac{\left(\frac{K_1 + K_2 + \bar{\Omega}}{|\mathbf{K}_1 + \mathbf{K}_2|} \right)^2 - \cos^2 \vartheta}{4\sqrt{\left(\frac{K_1 + K_2 + \bar{\Omega}}{|\mathbf{K}_1 + \mathbf{K}_2|} \right)^2 - 1}}.$$

For the parameters of our estimate ($\hbar\Omega = 0.35 \text{eV}$, $\lambda = 15 \text{eV}\text{\AA}$, $\bar{\mathcal{E}} \approx 4 \cdot 10^5 \text{V/m}$, $k_F = 1.2 \cdot 10^8 \text{m}^{-1}$), we find

$$\bar{\Omega} = 1.9.$$

A numerical evaluation of the remaining integral gives

$$\begin{aligned}\Gamma_{\text{int}} &\approx 1.02 \cdot 10^{-3} \cdot \frac{V^2(0) k_F^5}{\hbar\lambda} \left(\frac{e\mathcal{E}\lambda}{\hbar\Omega_F^2} \right)^2 \\ &= 1.02 \cdot 10^{-3} \cdot \frac{V^2(0) k_F^5}{\hbar\lambda} \left(\frac{e\mathcal{E}\lambda}{\hbar\Omega_F^2} \right)^2\end{aligned}$$

On the other hand

$$V(0) \approx \frac{e^2\pi}{2\varepsilon\alpha k_F}.$$

Collecting everything and assuming $\varepsilon = 6\varepsilon_0$, we find

$$\begin{aligned}\Gamma_{\text{int}} &\approx 1.02 \cdot 10^{-3} \cdot \frac{\pi e^4 k_F^3}{16\hbar\varepsilon^2\alpha^2\lambda} \left(\frac{e\mathcal{E}\lambda}{\hbar\Omega_F^2} \right)^2 \\ &\approx 0.49 \cdot 10^6 \text{ Hz} \cdot \rho,\end{aligned}$$

where we used our estimate

$$\frac{e\mathcal{E}\lambda}{\hbar\Omega_F^2} \approx 5 \cdot 10^{-3}.$$

3. Temperature estimate

We estimate the effective temperature of electrons using experimental data on the cooling power provided by phonons. In a Floquet driven system, the effective temperature of the electrons and the temperature of the lattice, which is coupled to a cold bath, can differ. The cooling power is the amount of energy per unit of time that is carried away by the cold lattice (mostly by optical phonons), thus stabilizing the effective electron temperature. While experimental results for the cooling power are available for graphene [97–99], theoretical work [101] shows that the cooling power of TMDs is even larger, leading to a lower effective temperature. Here, for a conservative estimate, we use the values measured for graphene [99], where the lattice was kept at 4.2 K.

The cooling power per electron P strongly depends on the effective temperature of the electrons. In two dimensional materials [100, 101] one finds

$$P_{\text{cool}} = \frac{\Sigma(\bar{\rho})}{\bar{\rho}} (T_e^4 - T_{\text{ph}}^4).$$

This law holds well for electron temperatures below 100 K. T_e is the effective electron temperature, and T_{ph} is the temperature of the lattice. The above assumes that the electrons are thermalized. In fact, one expects a very fast thermalization of the electrons due to electron–electron interactions. For the above estimate of $\bar{\rho} = 1.18 \cdot 10^{11}/\text{cm}^{-2}$, we find $\Sigma(\bar{\rho}) \approx 1 \frac{\text{mW}}{\text{K}^4\text{m}^2}$. On the other hand, the power supplied by Floquet drive is

$$P_{\text{drive}} = \hbar\Omega_F (\Gamma_{\text{int}} + \Gamma_\gamma) / \bar{\rho}.$$

Setting $P_{\text{cool}} = P_{\text{drive}}$, we find that cooling and heating rates are balanced at the effective electron temperature

$$T_e \approx 20 \text{ K}. \quad (\text{S } 22)$$

Eq. (S 22) shows that the heating induced by MFPD is not too large. In fact, due to the nonlinear dependence of the cooling power on T_e , the driving power could be easily increased by two orders of magnitude giving an effective temperature of only $T_e \approx 60 \text{ K}$.

4. Landau damping

The Landau damping of plasmons is described by the imaginary part of the Lindhard function

$$\chi(\omega, \mathbf{q}) = \int \frac{d^2k}{(2\pi)^2} \frac{f(\varepsilon_{\mathbf{k}-\mathbf{q}/2}) - f(\varepsilon_{\mathbf{k}+\mathbf{q}/2})}{\omega + i0^+ + \varepsilon_{\mathbf{k}-\mathbf{q}/2} - \varepsilon_{\mathbf{k}+\mathbf{q}/2}}.$$

The imaginary part is

$$\text{Im} [\chi(\omega, \mathbf{q})] = -\pi \int \frac{kdk}{(2\pi)^2} \int d\varphi [f(\varepsilon_{\mathbf{k}}) - f(\varepsilon_{\mathbf{k}+\mathbf{q}})] \delta(\omega + \varepsilon_{\mathbf{k}} - \varepsilon_{\mathbf{k}+\mathbf{q}}).$$

Let $\varepsilon_{\mathbf{k}} = k^2/2m^*$. This assumption simplifies the calculations but can be made without loss of generality, because in the end we only need to consider the linearized dispersion in the vicinity of the Fermi surface. Defining the quantities $\mathbf{K} = \mathbf{k}/\sqrt{2m^*}$, $\mathbf{Q}' = \mathbf{q}/\sqrt{2m^*}$ (not to be confused with the wavevector of the Goldstone-like modes, \mathbf{Q}), we have

$$\begin{aligned} \text{Im} [\chi(\omega, \mathbf{q})] &= -\pi \int \frac{kdk}{(2\pi)^2} \int d\varphi [f(K^2) - f(K^2 + Q'^2 + 2KQ' \cos \varphi)] \delta(Q'^2 + 2KQ' \cos \varphi - \omega) \\ &\quad - 2m^* \pi \int \frac{KdK}{(2\pi)^2} \int d\varphi [f(K^2) - f(K^2 + Q'^2 + 2KQ' \cos \varphi)] \delta\left(\frac{Q'^2 - \omega}{2KQ'} + \cos \varphi\right) \end{aligned}$$

We are interested in the case $\frac{Q'^2 - \omega}{2KQ'} < 0$, i.e. $-\pi/2 < \varphi < \pi/2$. We substitute

$$\begin{aligned} \mu &= \cos \varphi \\ d\varphi &= -\frac{d\mu}{\sin \varphi} = -\frac{d\mu}{\pm \sqrt{1 - \cos^2 \varphi}} \end{aligned}$$

where the plus-minus-sign indicates that we have to distinguish the cases $\varphi \lesseqgtr 0$. We find

$$\begin{aligned} \text{Im} [\chi(\omega, \mathbf{Q}')] &= -\frac{m^* \pi}{Q'} \int \frac{dK}{(2\pi)^2} \int_{-1}^1 \frac{d\mu}{\sqrt{1 - \mu^2}} [f(K^2) - f(K^2 + Q'^2 + 2KQ'\mu)] \delta\left(\frac{Q'^2 - \omega}{2KQ'} + \mu\right) \\ &= -\frac{m^* \pi}{Q'} \int_{\frac{\omega - Q^2}{2Q}}^{\infty} \frac{dK}{(2\pi)^2} \frac{1}{\sqrt{1 - \left(\frac{Q'^2 - \omega}{2KQ'}\right)^2}} [f(K^2) - f(K^2 + \omega)], \end{aligned} \quad (\text{S } 23)$$

where the last step follows from

$$-1 < \frac{Q'^2 - \omega}{2KQ'} < 0$$

For $T = 0$, approximating $f(K^2) - f(K^2 - \omega) \approx -\delta(K - K_F) \omega / K_F$, we find

$$\text{Im} [\chi(\omega, \mathbf{q})] = \frac{-m^* \omega}{4\pi Q K_F} \frac{\Theta\left(K_F - \frac{Q'^2 + \omega}{2Q}\right)}{\sqrt{1 - \frac{(Q'^2 - \omega)^2}{4K_F^2 Q'^2}}}$$

As the theta function indicates, plasmons are undamped for

$$\frac{qk_F}{m^*} < \omega - \frac{q^2}{2m}.$$

In our case $\omega \gg q^2/2m^*$ and the condition reduces to

$$\omega > v_F q.$$

At finite temperatures and with $\omega/Q' \gg Q'$, the integral in Eq. (S 23) can be approximated as

$$\text{Im} [\chi(\omega, \mathbf{q})] \approx -\frac{m^* \pi}{Q'} \int_{\frac{\omega}{2Q}}^{\infty} \frac{dK}{(2\pi)^2} \frac{K}{\sqrt{K^2 - \left(\frac{\omega}{2Q'}\right)^2}} [f(K^2) - f(K^2 + \omega)]$$

For $\omega \gg v_F q = K_F Q'/2$, we can approximate the Fermi-Dirac distributions as exponentials

$$\begin{aligned}
\text{Im} [\chi(\omega, \mathbf{q})] &\approx -\frac{m^* \pi}{Q'} \int_{\frac{\omega}{2Q}}^{\infty} \frac{dK}{(2\pi)^2} \frac{K}{\sqrt{K^2 - \left(\frac{\omega}{2Q}\right)^2}} \left[e^{-\beta K^2} - e^{-\beta(K^2 + \omega)} \right] \\
&= -\frac{m^* \pi}{(2\pi)^2 Q'} \int_{\left(\frac{\omega}{2Q'}\right)^2}^{\infty} dE \frac{1}{\sqrt{E - \left(\frac{\omega}{2Q'}\right)^2}} \left[e^{-\beta E} - e^{-\beta(E + \omega)} \right] \\
&\approx -\frac{m^* \omega}{4\pi Q'} \int_{\left(\frac{\omega}{2Q'}\right)^2}^{\infty} dE \frac{\beta e^{-\beta E}}{\sqrt{E - \left(\frac{\omega}{2Q'}\right)^2}} = -\frac{m^* \omega}{4\pi Q'} \sqrt{\beta} \int_{\beta \left(\frac{\omega}{2Q'}\right)^2}^{\infty} dx \frac{e^{-x}}{\sqrt{x - \beta \left(\frac{\omega}{2Q'}\right)^2}} \\
&= -\frac{m^* \omega}{4\pi Q'} \sqrt{\beta} e^{-\beta \left(\frac{\omega}{2Q'}\right)^2} \int_0^{\infty} dx \frac{e^{-x}}{\sqrt{x}} \\
&= -\frac{m^* \omega \sqrt{\beta}}{4\sqrt{\pi} Q'} e^{-\beta \left(\frac{\omega}{2Q'}\right)^2} \tag{S 24}
\end{aligned}$$

Let us finally estimate a numerical value for the Landau damping induced by MFPD. To find the factor $e^{-\beta \left(\frac{\omega}{2Q}\right)^2}$ in Eq. (S 24), we assume $T = 300 K$ which is much larger than the MFPD induced temperature rise. This is an overestimate, as the temperature as well as the Landau damping will be smaller in a typical experiment (performed at liquid nitrogen temperatures, e.g.). For a plasmon with wavelength $1\mu m$ and roughly $\omega = 1$ THz, we find

$$\beta \left(\frac{\sqrt{m^*} \omega}{2q} \right)^2 \sim 10^3,$$

such that even at room temperature, the Landau damping is suppressed by a factor of

$$\sim e^{-10^3}.$$

-
- [1] A. Cavalleri, *Photo-induced superconductivity*, Contemporary Physics **59**, 31 (2018).
 - [2] D. Fausti, R. Tobey, N. Dean, S. Kaiser, A. Dienst, M. C. Hoffmann, S. Pyon, T. Takayama, H. Takagi, and A. Cavalleri, *Light-induced superconductivity in a stripe-ordered cuprate*, science **331**, 189 (2011).
 - [3] M. Först, R. Tobey, S. Wall, H. Bromberger, V. Khanna, A. L. Cavalieri, Y.-D. Chuang, W. Lee, R. Moore, W. Schlotter *et al.*, *Driving magnetic order in a manganite by ultrafast lattice excitation*, Physical Review B **84**, 241104 (2011).
 - [4] M. Rini, R. Tobey, N. Dean, J. Itatani, Y. Tomioka, Y. Tokura, R. W. Schoenlein, and A. Cavalleri, *Control of the electronic phase of a manganite by mode-selective vibrational excitation*, Nature **449**, 72 (2007).
 - [5] M. S. Rudner and J. C. Song, *Self-induced berry flux and spontaneous non-equilibrium magnetism*, Nature Physics **15**, 1017 (2019).
 - [6] M. Faraday, *On a peculiar class of acoustical figures; and on certain forms assumed by groups of particles upon vibrating elastic surfaces*, Philosophical transactions of the Royal Society of London (299–340) (1831).
 - [7] T. B. Benjamin and F. J. Ursell, *The stability of the plane free surface of a liquid in vertical periodic motion*, Proceedings of the Royal Society of London. Series A. Mathematical and Physical Sciences **225**, 505 (1954).
 - [8] K. Kumar and L. S. Tuckerman, *Parametric instability of the interface between two fluids*, Journal of Fluid Mechanics **279**, 49 (1994).
 - [9] T. Oka and H. Aoki, *Photovoltaic hall effect in graphene*, Physical Review B **79**, 081406 (2009).
 - [10] T. Kitagawa, T. Oka, A. Brataas, L. Fu, and E. Demler, *Transport properties of nonequilibrium systems under the application of light: Photoinduced quantum hall insulators without landau levels*, Physical Review B **84**, 235108 (2011).
 - [11] N. H. Lindner, G. Refael, and V. Galitski, *Floquet topological insulator in semiconductor quantum wells*, Nature Physics **7**, 490 (2011).
 - [12] Y. Wang, H. Steinberg, P. Jarillo-Herrero, and N. Gedik, *Observation of floquet-bloch states on the surface of a topological insulator*, Science **342**, 453 (2013).
 - [13] F. Mahmood, C.-K. Chan, Z. Alpichshev, D. Gardner, Y. Lee, P. A. Lee, and N. Gedik, *Selective scattering between floquet-bloch and volkov states in a topological insulator*, Nature Physics **12**, 306 (2016).
 - [14] J. W. McIver, B. Schulte, F.-U. Stein, T. Matsuyama, G. Jotzu, G. Meier, and A. Cavalleri, *Light-induced anomalous hall effect in graphene*, Nature physics **16**, 38 (2020).

- [15] T. Kitagawa, E. Berg, M. Rudner, and E. Demler, *Topological characterization of periodically driven quantum systems*, Physical Review B **82**, 235114 (2010).
- [16] S. Zhou, C. Bao, B. Fan, H. Zhou, Q. Gao, H. Zhong, T. Lin, H. Liu, P. Yu, P. Tang *et al.*, *Pseudospin-selective floquet band engineering in black phosphorus*, Nature **614**, 75 (2023).
- [17] G. Usaj, P. M. Perez-Piskunow, L. F. Torres, and C. A. Balseiro, *Irradiated graphene as a tunable floquet topological insulator*, Physical Review B **90**, 115423 (2014).
- [18] P. M. Perez-Piskunow, G. Usaj, C. A. Balseiro, and L. F. Torres, *Floquet chiral edge states in graphene*, Physical Review B **89**, 121401 (2014).
- [19] T. Oka and S. Kitamura, *Floquet engineering of quantum materials*, Annual Review of Condensed Matter Physics **10**, 387 (2019).
- [20] O. Katz, G. Refael, and N. H. Lindner, *Optically induced flat bands in twisted bilayer graphene*, Physical Review B **102**, 155123 (2020).
- [21] I. Esin, M. S. Rudner, G. Refael, and N. H. Lindner, *Quantized transport and steady states of floquet topological insulators*, Physical Review B **97**, 245401 (2018).
- [22] I. Esin, M. S. Rudner, and N. H. Lindner, *Floquet metal-to-insulator phase transitions in semiconductor nanowires*, Science advances **6**, eaay4922 (2020).
- [23] I. Esin, G. K. Gupta, E. Berg, M. S. Rudner, and N. H. Lindner, *Electronic floquet gyro-liquid crystal*, Nature communications **12**, 1 (2021).
- [24] H. Dehghani, T. Oka, and A. Mitra, *Out-of-equilibrium electrons and the hall conductance of a floquet topological insulator*, Physical Review B **91**, 155422 (2015).
- [25] M. Genske and A. Rosch, *Floquet-boltzmann equation for periodically driven fermi systems*, Physical Review A **92**, 062108 (2015).
- [26] L. Glazman, *Kinetics of electrons and holes in direct-gap semiconductors photo-excited by high-intensity pulses*, Soviet Physics Semiconductors-USSR **17**, 494 (1983).
- [27] H. Dehghani, T. Oka, and A. Mitra, *Dissipative floquet topological systems*, Physical Review B **90**, 195429 (2014).
- [28] M. Sentef, M. Claassen, A. Kemper, B. Moritz, T. Oka, J. Freericks, and T. Devereaux, *Theory of floquet band formation and local pseudospin textures in pump-probe photoemission of graphene*, Nature communications **6**, 7047 (2015).
- [29] C.-K. Chan, P. A. Lee, K. S. Burch, J. H. Han, and Y. Ran, *When chiral photons meet chiral fermions: photoinduced anomalous hall effects in weyl semimetals*, Physical review letters **116**, 026805 (2016).
- [30] A. Farrell and T. Pereg-Barnea, *Photon-inhibited topological transport in quantum well heterostructures*, Physical Review Letters **115**, 106403 (2015).
- [31] Z. Gu, H. Fertig, D. P. Arovas, and A. Auerbach, *Floquet spectrum and transport through an irradiated graphene ribbon*, Physical review letters **107**, 216601 (2011).
- [32] H. Hübener, M. A. Sentef, U. De Giovannini, A. F. Kemper, and A. Rubio, *Creating stable floquet–weyl semimetals by laser-driving of 3d dirac materials*, Nature communications **8**, 13940 (2017).
- [33] L. Jiang, T. Kitagawa, J. Alicea, A. Akhmerov, D. Pekker, G. Refael, J. I. Cirac, E. Demler, M. D. Lukin, and P. Zoller, *Majorana fermions in equilibrium and in driven cold-atom quantum wires*, Physical review letters **106**, 220402 (2011).
- [34] D. M. Kennes, N. Müller, M. Pletyukhov, C. Weber, C. Bruder, F. Hassler, J. Klinovaja, D. Loss, and H. Schoeller, *Chiral one-dimensional floquet topological insulators beyond the rotating wave approximation*, Physical Review B **100**, 041103 (2019).
- [35] A. Kundu and B. Seradjeh, *Transport signatures of floquet majorana fermions in driven topological superconductors*, Physical review letters **111**, 136402 (2013).
- [36] M. Thakurathi, D. Loss, and J. Klinovaja, *Floquet majorana fermions and parafermions in driven rashba nanowires*, Physical Review B **95**, 155407 (2017).
- [37] R. Frank, *Quantum criticality and population trapping of fermions by non-equilibrium lattice modulations*, New Journal of Physics **15**, 123030 (2013).
- [38] A. Castro, U. De Giovannini, S. A. Sato, H. Hübener, and A. Rubio, *Floquet engineering the band structure of materials with optimal control theory*, Physical Review Research **4**, 033213 (2022).
- [39] O. Neufeld, A. Fleischer, and O. Cohen, *High-order harmonic generation of pulses with multiple timescales: selection rules, carrier envelope phase and cutoff energy*, Molecular Physics **117**, 1956 (2019).
- [40] O. Neufeld, D. Podolsky, and O. Cohen, *Floquet group theory and its application to selection rules in harmonic generation*, Nature communications **10**, 405 (2019).
- [41] Y. Ikeda, S. Kitamura, and T. Morimoto, *Floquet engineering of electric polarization with two-frequency drive*, Progress of Theoretical and Experimental Physics **2022**, 04A101 (2022).
- [42] D. Basov, R. Averitt, and D. Hsieh, *Towards properties on demand in quantum materials*, Nature materials **16**, 1077 (2017).
- [43] J. Bloch, A. Cavalleri, V. Galitski, M. Hafezi, and A. Rubio, *Strongly correlated electron–photon systems*, Nature **606**, 41 (2022).
- [44] J. Mentink, K. Balzer, and M. Eckstein, *Ultrafast and reversible control of the exchange interaction in mott insulators*, Nature communications **6**, 6708 (2015).
- [45] M. Dykman, C. Bruder, N. Lörch, and Y. Zhang, *Interaction-induced time-symmetry breaking in driven quantum oscillators*, Physical Review B **98**, 195444 (2018).
- [46] K. Kim, M.-S. Heo, K.-H. Lee, K. Jang, H.-R. Noh, D. Kim, and W. Jhe, *Spontaneous symmetry breaking of population in a nonadiabatically driven atomic trap: an ising-class phase transition*, Physical review letters **96**, 150601 (2006).

- [47] M.-S. Heo, Y. Kim, K. Kim, G. Moon, J. Lee, H.-R. Noh, M. Dykman, and W. Jhe, *Ideal mean-field transition in a modulated cold atom system*, Physical Review E **82**, 031134 (2010).
- [48] A. Kyprianidis, F. Machado, W. Morong, P. Becker, K. S. Collins, D. V. Else, L. Feng, P. W. Hess, C. Nayak, G. Pagano *et al.*, *Observation of a prethermal discrete time crystal*, Science **372**, 1192 (2021).
- [49] M. S. Rudner and N. H. Lindner, *Band structure engineering and non-equilibrium dynamics in floquet topological insulators*, Nature reviews physics **2**, 229 (2020).
- [50] D. V. Else, B. Bauer, and C. Nayak, *Floquet time crystals*, Physical review letters **117**, 090402 (2016).
- [51] N. Y. Yao, A. C. Potter, I.-D. Potirniche, and A. Vishwanath, *Discrete time crystals: Rigidity, criticality, and realizations*, Physical review letters **118**, 030401 (2017).
- [52] J. Zhang, P. W. Hess, A. Kyprianidis, P. Becker, A. Lee, J. Smith, G. Pagano, I.-D. Potirniche, A. C. Potter, A. Vishwanath *et al.*, *Observation of a discrete time crystal*, Nature **543**, 217 (2017).
- [53] S. Choi, J. Choi, R. Landig, G. Kucsko, H. Zhou, J. Isoya, F. Jelezko, S. Onoda, H. Sumiya, V. Khemani *et al.*, *Observation of discrete time-crystalline order in a disordered dipolar many-body system*, Nature **543**, 221 (2017).
- [54] M. Natsheh, A. Gambassi, and A. Mitra, *Critical properties of the prethermal floquet time crystal*, Physical Review B **103**, 224311 (2021).
- [55] A. Lazarides, A. Das, and R. Moessner, *Equilibrium states of generic quantum systems subject to periodic driving*, Physical Review E **90**, 012110 (2014).
- [56] L. D'Alessio and M. Rigol, *Long-time behavior of isolated periodically driven interacting lattice systems*, Physical Review X **4**, 041048 (2014).
- [57] M. Bukov, M. Heyl, D. A. Huse, and A. Polkovnikov, *Heating and many-body resonances in a periodically driven two-band system*, Physical Review B **93**, 155132 (2016).
- [58] M. Bukov, L. D'Alessio, and A. Polkovnikov, *Universal high-frequency behavior of periodically driven systems: from dynamical stabilization to floquet engineering*, Advances in Physics **64**, 139 (2015).
- [59] D. V. Else, B. Bauer, and C. Nayak, *Prethermal phases of matter protected by time-translation symmetry*, Physical Review X **7**, 011026 (2017).
- [60] T. Mori, *Floquet prethermalization in periodically driven classical spin systems*, Physical Review B **98**, 104303 (2018).
- [61] M. Reitter, J. Näger, K. Wintersperger, C. Sträter, I. Bloch, A. Eckardt, and U. Schneider, *Interaction dependent heating and atom loss in a periodically driven optical lattice*, Physical review letters **119**, 200402 (2017).
- [62] K. Singh, C. J. Fujiwara, Z. A. Geiger, E. Q. Simmons, M. Lipatov, A. Cao, P. Dotti, S. V. Rajagopal, R. Senaratne, T. Shimasaki *et al.*, *Quantifying and controlling prethermal nonergodicity in interacting floquet matter*, Physical Review X **9**, 041021 (2019).
- [63] V. Galitsky, S. Goreslavsky, and V. Elesin, *Electric and magnetic properties of a semiconductor in the field of a strong electromagnetic wave*, SOV PHYS JETP **30**, 117 (1970).
- [64] T. Shirai, T. Mori, and S. Miyashita, *Condition for emergence of the floquet-gibbs state in periodically driven open systems*, Physical Review E **91**, 030101 (2015).
- [65] K. I. Seetharam, C.-E. Bardyn, N. H. Lindner, M. S. Rudner, and G. Refael, *Controlled population of floquet-bloch states via coupling to bose and fermi baths*, Physical Review X **5**, 041050 (2015).
- [66] T. Iadecola, T. Neupert, and C. Chamon, *Occupation of topological floquet bands in open systems*, Physical Review B **91**, 235133 (2015).
- [67] K. I. Seetharam, C.-E. Bardyn, N. H. Lindner, M. S. Rudner, and G. Refael, *Steady states of interacting floquet insulators*, Physical Review B **99**, 014307 (2019).
- [68] D. E. Liu, *Classification of the floquet statistical distribution for time-periodic open systems*, Physical Review B **91**, 144301 (2015).
- [69] D. A. Abanin, W. De Roeck, and F. Huveneers, *Exponentially slow heating in periodically driven many-body systems*, Physical review letters **115**, 256803 (2015).
- [70] A. Eguiluz and J. Quinn, *Hydrodynamic model for surface plasmons in metals and degenerate semiconductors*, Physical Review B **14**, 1347 (1976).
- [71] D. Pines and P. Nozières, *Theory Of Quantum Liquids: Normal Fermi Liquids*, CRC Press (1989). ISBN 978-0201407747.
- [72] U. Briskot, M. Schütt, I. V. Gornyi, M. Titov, B. N. Narozhny, and A. D. Mirlin, *Collision-dominated nonlinear hydrodynamics in graphene*, Phys. Rev. B **92**, 115426 (2015).
- [73] D. Forster, *Hydrodynamic Fluctuations, Broken Symmetry, and Correlation Functions*, CRC Press (2018). ISBN 978-0367091323.
- [74] L. D. Landau and E. M. Lifshits, *Fluid mechanics*, Butterworth-Heinemann (1987). ISBN 978-0750627672.
- [75] A. Lucas and S. Sachdev, *Memory matrix theory of magnetotransport in strange metals*, Physical Review B **91**, 195122 (2015).
- [76] L. D. Landau and E. M. Lifshitz, *Mechanics*, Butterworth-Heinemann (1976). ISBN 978-0750628969.
- [77] A. Lucas and S. D. Sarma, *Electronic sound modes and plasmons in hydrodynamic two-dimensional metals*, Phys. Rev. B **97**, 115449 (2018).
- [78] E. I. Kiselev, *Universal superdiffusive modes in charged two dimensional liquids*, Physical Review B **103**, 235116 (2021).
- [79] The Fourier transform of the Coulomb potential is $V(q) = 2\pi/q$ and is responsible for the characteristic $\sim \sqrt{q}$ dispersion of two dimensional plasmons, whereas the pressure term scales as $\sim q$ and will only contribute a small correction.
- [80] G. Ni, d. A. McLeod, Z. Sun, L. Wang, L. Xiong, K. Post, S. Sunku, B.-Y. Jiang, J. Hone, C. R. Dean *et al.*, *Fundamental limits to graphene plasmonics*, Nature **557**, 530 (2018).
- [81] A. Principi, G. Vignale, M. Carrega, and M. Polini, *Intrinsic lifetime of dirac plasmons in graphene*, Physical Review B

- 88**, 195405 (2013).
- [82] M. Lyubarov, Y. Lumer, A. Dikopoltsev, E. Lustig, Y. Sharabi, and M. Segev, *Amplified emission and lasing in photonic time crystals*, *Science* **377**, 425 (2022).
- [83] E. Galiffi, R. Tirole, S. Yin, H. Li, S. Vezzoli, P. A. Huidobro, M. G. Silveirinha, R. Sapienza, A. Alù, and J. Pendry, *Photonics of time-varying media*, *Advanced Photonics* **4**, 014002 (2022).
- [84] Z. Sun, D. Basov, and M. Fogler, *Graphene as a source of entangled plasmons*, *Physical Review Research* **4**, 023208 (2022).
- [85] K. J. Burns, G. M. Vasil, J. S. Oishi, D. Lecoanet, and B. P. Brown, *Dedalus: A flexible framework for numerical simulations with spectral methods*, *Physical Review Research* **2**, 023068 (2020).
- [86] V. E. Zakharov, V. S. L'vov, and S. S. Starobinets, *Spin-wave turbulence beyond the parametric excitation threshold*, *Soviet Physics Uspekhi* **17**, 896 (1975).
- [87] W. S. Edwards and S. Fauve, *Patterns and quasi-patterns in the faraday experiment*, *Journal of Fluid Mechanics* **278**, 123 (1994).
- [88] H. W. Müller, *Model equations for two-dimensional quasipatterns*, *Physical Review E* **49**, 1273 (1994).
- [89] P. Chen and J. Vinals, *Pattern selection in faraday waves*, *Physical Review Letters* **79**, 2670 (1997).
- [90] P. Chen and J. Vinals, *Amplitude equation and pattern selection in faraday waves*, *Physical Review E* **60**, 559 (1999).
- [91] A. Di Carli, R. Cruickshank, M. Mitchell, A. La Rooij, S. Kuhr, C. E. Creffield, and E. Haller, *Instabilities of interacting matter waves in optical lattices with floquet driving*, arXiv preprint arXiv:2303.06092 (2023).
- [92] N. Dupont, L. Gabardos, F. Arrouas, G. Chatelain, M. Arnal, J. Billy, P. Schlagheck, B. Peaudecerf, and D. Guéry-Odelin, *Emergence of a tunable crystalline order in a floquet-bloch system from a parametric instability*, arXiv preprint arXiv:2212.10890 (2022).
- [93] S. Fazzini, P. Chudzinski, C. Dauer, I. Schneider, and S. Eggert, *Nonequilibrium floquet steady states of time-periodic driven luttinger liquids*, *Physical Review Letters* **126**, 243401 (2021).
- [94] M. Dykman, C. Maloney, V. Smelyanskiy, and M. Silverstein, *Fluctuational phase-flip transitions in parametrically driven oscillators*, *Physical Review E* **57**, 5202 (1998).
- [95] M. Marthaler and M. Dykman, *Switching via quantum activation: A parametrically modulated oscillator*, *Physical Review A* **73**, 042108 (2006).
- [96] L. Domino, M. Tarpin, S. Patinet, and A. Eddi, *Faraday wave lattice as an elastic metamaterial*, *Physical Review E* **93**, 050202 (2016).
- [97] A. Baker, J. Alexander-Webber, T. Altbaeumer, and R. Nicholas, *Energy relaxation for hot dirac fermions in graphene and breakdown of the quantum hall effect*, *Physical review B* **85**, 115403 (2012).
- [98] A. Baker, J. Alexander-Webber, T. Altbaeumer, S. McMullan, T. Janssen, A. Tzalenchuk, S. Lara-Avila, S. Kubatkin, R. Yakimova, C.-T. Lin *et al.*, *Energy loss rates of hot dirac fermions in epitaxial, exfoliated, and cvd graphene*, *Physical Review B* **87**, 045414 (2013).
- [99] A. Betz, F. Violla, D. Brunel, C. Voisin, M. Picher, A. Cavanna, A. Madouri, G. Fève, J.-M. Berroir, B. Plaçais *et al.*, *Hot electron cooling by acoustic phonons in graphene*, *Physical Review Letters* **109**, 056805 (2012).
- [100] S. Kubakaddi, *Interaction of massless dirac electrons with acoustic phonons in graphene at low temperatures*, *Physical Review B* **79**, 075417 (2009).
- [101] K. Kaasbjerg, K. Bhargavi, and S. Kubakaddi, *Hot-electron cooling by acoustic and optical phonons in monolayers of mos 2 and other transition-metal dichalcogenides*, *Physical Review B* **90**, 165436 (2014).
- [102] T. Low and P. Avouris, *Graphene plasmonics for terahertz to mid-infrared applications*, *ACS nano* **8**, 1086 (2014).
- [103] A. Chaves, J. G. Azadani, H. Alsalman, D. Da Costa, R. Frisenda, A. Chaves, S. H. Song, Y. D. Kim, D. He, J. Zhou *et al.*, *Bandgap engineering of two-dimensional semiconductor materials*, *npj 2D Materials and Applications* **4**, 1 (2020).
- [104] A. Chaves, R. Ribeiro, T. Frederico, and N. Peres, *Excitonic effects in the optical properties of 2d materials: an equation of motion approach*, *2D Materials* **4**, 025086 (2017).
- [105] M. Merboldt, M. Schüler, D. Schmitt, J. P. Bange, W. Bennecke, K. Gadge, K. Pierz, H. W. Schumacher, D. Momeni, D. Steil, S. R. Manmana, M. Sentef, M. Reutzler, and S. Mathias, *Observation of floquet states in graphene*, arXiv preprint arXiv:2404.12791 (2024).
- [106] D. Choi, M. Mogi, U. De Giovannini, D. Azoury, B. Lv, Y. Su, H. Hübener, A. Rubio, and N. Gedik, *Direct observation of floquet-bloch states in monolayer graphene*, arXiv preprint arXiv:2404.14392 (2024).
- [107] S. Manzeli, D. Ovchinnikov, D. Pasquier, O. V. Yazyev, and A. Kis, *2d transition metal dichalcogenides*, *Nature Reviews Materials* **2**, 1 (2017).
- [108] E. Lustig, Y. Sharabi, and M. Segev, *Topological aspects of photonic time crystals*, *Optica* **5**, 1390 (2018).
- [109] S. Shin, N. Kim, J. Kim, K. Kim, D. Noh, K. S. Kim, and J. Chung, *Control of the π plasmon in a single layer graphene by charge doping*, *Applied Physics Letters* **99**, 082110 (2011).
- [110] J. Chen, M. Badioli, P. Alonso-González, S. Thongrattanasiri, F. Huth, J. Osmond, M. Spasenović, A. Centeno, A. Pesquera, P. Godignon, A. Z. Elorza, N. Camara, F. J. Garc a de Abajo, R. Hillenbrand, and F. H. L. Koppens, *Optical nano-imaging of gate-tunable graphene plasmons*, *Nature* **487**, 77 (2012).
- [111] Z. Fei, A. Rodin, G. O. Andreev, W. Bao, A. McLeod, M. Wagner, L. Zhang, Z. Zhao, M. Thiemens, G. Dominguez, M. M. Fogler, A. H. Castro Neto, C. N. Lau, F. Keilmann, and D. N. Basov, *Gate-tuning of graphene plasmons revealed by infrared nano-imaging*, *Nature* **487**, 82 (2012).
- [112] A. Pertsova and A. V. Balatsky, *Excitonic instability in optically pumped three-dimensional dirac materials*, *Physical Review B* **97**, 075109 (2018).
- [113] S. Sachdev, *Nonzero-temperature transport near fractional quantum hall critical points*, *Physical Review B* **57**, 7157 (1998).